

Influence of Filler Wires to Suppress the Microsegregation and to Improve Mechanical Properties of Conventional Arc-Welded Nickel-Based Superalloy Incoloy 20

M. Natesh¹ · M. Manikandan¹

Received: 8 October 2019 / Accepted: 3 April 2020 / Published online: 12 May 2020
© The Indian Institute of Metals - IIM 2020

Abstract Elemental segregation leads to hot fissuring in the Incoloy 20. The present investigation examines the possibility of lessening the elemental segregation in the conventional arc welding techniques. In the present investigation, Incoloy 20 plates were fused by continuous current gas tungsten arc welding (CCGTAW) and pulsed current gas tungsten arc welding (PCGTAW) with two different nickel-based filler wires (ERNiCrMo-2 and ERNiCrMo-3). The result of the macroexamination shows that steady fluid flow with crack-free welding was succeeded in all the weldments. Optical and scanning electron microscope proves the columnar and cellular structure in CCGTAW specimens and fine equiaxed dendritic structure in PCGTAW specimens. Energy-dispersive spectroscopy (EDS) and X-ray diffraction results exhibit that the weld joint produced by CCGTAW ERNiCrMo-2 shows Cr segregation that leads to the formation of $M_{23}C_6$ phases in the interdendritic regions, whereas ERNiCrMo-3 shows the presence of NbC instead of $M_{23}C_6$. The elemental segregation is suppressed when it comes to PCGTAW weldments in both filler wires. Electron backscatter diffraction analysis shows that the CCGTAW weldments show coarser grain structure in the heat-affected zone (HAZ). In all the cases, the formation of secondary phases affects the strength of the weld joints at HAZ. Refined microstructure obtained in the PCGTAW in both filler wires shows the marginally higher ultimate tensile strength and toughness compared to

the corresponding CCGTAW weldments. From the corrosion study, PCGTAW specimens exhibit higher corrosion resistance than the CCGTAW specimens for both filler wires.

Keywords Incoloy20 · Microsegregation · Pulsed current gas tungsten arc welding · Microstructure · Corrosion · Mechanical properties

1 Introduction

Incoloy 20 [UNS N08020 (ASTM A240)] is a nickel-based austenitic superalloy derived from Ni–Fe–Cr ternary system. Incoloy 20 is a single crystal structure with the austenitic phase. It is a precipitation-strengthened superalloy. Precipitation strengthening is obtained by adding a minor amount of alloying elements like Nb, Ti, and Al. These alloying elements lead to produce gamma prime precipitates such as Ni_3Al , $Ni_3(Al, Ti)$, and Ni_3Ti . This alloy was developed to provide excellent resistance to corrosion at elevated temperature in an acid medium like sulfuric acid, chlorides, phosphoric acid, and nitric acid. Incoloy 20 is also widely used in many industrial applications like heat exchangers, pickling equipment, process piping, mixing tanks, valves, fasteners, fitting, and pumps [1, 2]. Also, the resistance to corrosion in the aqueous environment is the same as alloy 825. Welding plays an imperative role in the fabrication industries to produce components in the aforesaid applications.

In general, industries are widely used shield metal arc welding (SMAW), gas metal arc welding (GMAW), and gas tungsten arc welding (GTAW) to fabricate the component out of this alloy [2]. These arc welding methods are inexpensive in comparison with other welding methods.

✉ M. Manikandan
mano.manikandan@gmail.com

M. Natesh
mvnatesh@gmail.com

¹ School of Mechanical Engineering, Vellore Institute of Technology, Vellore 632014, India

However, many researchers reported that the welding of Ni–Fe–Cr-based alloys using conventional arc welding processes leads to several problems [3, 4]. Navid Sayyar et al. [5] investigated the arc welding of Incoloy 825 to stainless steel AISI 321 welds with three variety of filler wires (Inconel 625, ER347, and Incoloy 65). Authors carried out EDS analysis to evaluate the elemental segregation; the results show that the elemental segregation tends to form the secondary phases in the grain boundaries of all the weldments. Authors observed the cracking due to the segregation of niobium (20.05 wt%) in the ER347 weldment. Inconel 625 provides good resistance to solidification cracking among the three filler wires, which are identified through the Varestraint test. Sayiram and Arivazhagan [6] investigated the microstructural evaluation of dissimilar welds between Incoloy 800H and AISI 321 austenitic stainless steel using the gas tungsten arc welding with two different nickel-based superalloy filler wires such as Inconel 82 and 617. Chromium-rich secondary phases are observed through EDS analysis at the interface of Incoloy 800H. The authors observed a reduction in mechanical properties due to secondary phases. The study concluded that Inconel 617 is the preferable filler metal to join the alloy between 800H and 321 stainless steel. Kangazian et al. [7] discussed the comparison between the continuous and pulsed current tungsten inert gas welding of dissimilar weld with SAF 2507 and Incoloy 825. The character of the microstructure on the corrosion properties of the weld metals is studied through potentiodynamic corrosion tester. The bimetallic joint with three varieties of filler wires (ERNiCrMo-3, ER2594, and ERNiFeCr-1) is carried out. The segregation of Mo (8.25%) in ERNiCrMo-3 and Ti (1%) segregation in ERNiFeCr-1 filler wires is noticed. The elemental segregation enhances the corrosion resistance of the weld joints. It is concluded that PCGTAW offers good resistance to corrosion in comparison with the CCGTAW technique. Dehmolaei et al. [8] reported the microstructural examination of the dissimilar weld between alloy 800 and HP. The welding is performed with tungsten inert gas welding with three different classes of filler wires (309 stainless steel, Inconel 617, and Inconel 82). The dendritic microstructures in all the weldments are observed. Transmission electron microscopy confirms the precipitation of $M_{23}C_6$ (Mo and Cr) and TiC is noticed in the weldment of 617. The authors noticed that a reduction in the mechanical properties occur due to $M_{23}C_6$ (Mo and Cr) precipitates. It is observed from the aforementioned literature that the major issues related to Ni–Fe–Cr-based superalloys are the formation of $M_{23}C_6$ (Mo and Cr) secondary phases. The segregation of Cr during solidification leads to Cr-depleted zone around the grain boundary. This affects the corrosion resistance of the alloy. These phases also lead to hot fissuring in the weldment [9, 10]. The

chemical composition of Incoloy 20 is similar to Incoloy 800, 800H, and 825 with minor modification of alloying elements. There is no study reported on the similar and dissimilar welding of Incoloy 20. It is essential to investigate the behavior of Incoloy 20 weldment fabricated by arc welding method. The appropriate selection of filler material and welding method is necessary to eliminate the microsegregation of alloying elements. Srikanth and Manikandan [11] attempted the comparative studies on GTA and PCGTA welding of alloy 600. The major issue related to the alloy 600 is the formation of $M_{23}C_6$ phases, which is similar to Incoloy 20. Welding with a variety of filler wires, which includes ERNiCrMo-3 filler wire, is carried out. Cr-rich $M_{23}C_6$ phases are completely suppressed in the pulsed current tungsten inert gas welding technique.

Mohammed Amir et al. [12] reported the investigation on electron beam welded Inconel 617 to AISI 310. The authors studied the microstructure and corrosion properties of the weldment. EDS analysis exhibits the segregation of Mo, Nb, Cr, and Co elements in the weld metal. The electrochemical corrosion test reveals that reduced pitting corrosion resistance of the weld metal is observed due to the segregation of Cr and Mo elements.

Cherish Mani et al. [13] discussed the cryogenically treated dissimilar welded stainless steel 316L and Monel 400 using the arc welding process (GTAW) for heat exchanger. The microstructure (OM, SEM with EDS) and corrosion properties (potentiodynamic polarization test) of the weldments are studied. Weld zone is observed with segregation of Fe, Cr, Cu, and Ni elements which leads to reduce the corrosion resistance of the weldment.

In the present study, two nickel-based filler wires such as ERNiCrMo-2 and ERNiCrMo-3 filler wires are adopted to produce the Incoloy 20 weld joints with continuous and pulsed current gas tungsten arc welding (PCGTAW) techniques. Commonly, the selection of filler metal is the most imperative weldment design. Welding can be carried out with (i) composition equal to base metal composition and (ii) overalloyed filler wire, i.e., higher than the base metal composition. Overalloyed filler wire has been employed for the high temperature application to resolve the elemental segregation. ERNiCrMo-2 filler wire is considered as an overalloyed filler metal. The elemental composition of Ni and Mo in the filler wire is greater than the base metal (Incoloy 20). ERNiCrMo-2 provides good corrosion resistance and strength at medium to high-temperature environment. Also, this filler wire is developed for high temperature application [14, 15]. ERNiCrMo-3 is the suggested filler wire by Special Metal for Incoloy 20. The presence of Nb (3.5 wt%) in the filler forms NbC instead of Cr-rich $M_{23}C_6$ secondary phases in the weldments. The presence of Nb and Ti in the filler metal (ERNiCrMo-3)

hinders the precipitation of chromium carbide in the weld metal (WM) [11]. So far, there is no literature reported on the aforesaid filler wires on Incoloy 20. In the present investigation, the welding characteristics of two different filler wires with CCGTA and PCGTA welding processes are performed. Many researchers [16, 17] reported that pulsed current tungsten inert gas welding supports to lessen elemental segregation. Similar benefits while welding of Incoloy 20 are expected.

Based on the reported literature on Ni–Fe–Cr based superalloy, it is observed that welding on Incoloy 20 is not reported so far. It is vital to develop the arc welding method to suppress the microsegregation of Cr and Mo to avoid the formation of $M_{23}C_6$ in the Incoloy 20 weldments. The objective of this study is to lessen the elemental segregation to improve the microstructural, mechanical, and corrosion properties of weldments fabricated with both filler wires using CCGTAW and PCGTAW. It is expected that the pulsed current gas tungsten arc welding improves the properties of the weld joint by lessening the magnitude of elemental segregation in comparison with gas tungsten arc welding. Outcomes of this investigation will be extremely valuable for the usages allied to this alloy in chemical environments.

2 Materials and Methodology for Welding and Characterization of Incoloy 20

2.1 Base Metal and Filler Wires

Hot-rolled and solution-annealed Incoloy 20 plate with a thickness of 5 mm was utilized in the present study. The elemental composition of the base metal and filler wires was tested, and the results are provided in Table 1. Two different Ni-based filler wires such as ERNiCrMo-2 and ERNiCrMo-3 with diameter of 1.6 mm were used in the present study to fabricate the weldment using CCGTAW and PCGTAW techniques.

2.2 Welding of Incoloy 20

Continuous and pulsed current gas tungsten arc welding was carried out using KEMPPII DWE 400 machine. Experimental trials were carried out in the manual mode with the polarity of the direct current electrode negative (DCEN). Weld plates were prepared in a specific dimension, which was $170 \times 70 \times 5$ mm. The preparation of the specimen was carefully made with appropriate dimensions (V-groove with 60° angle and landing of 1.5 mm). To protect the weldment in the environment, argon was adopted as a shielding gas with a steady flow rate (15 L/min). The welded plates are shown in Fig. 1.

The process parameters and heat input calculations involved in the present investigation are provided in Tables 2 and 3 for CCGTAW and PCGTAW processes, respectively. In the CCGTAW, the heat input was computed from the constant current, whereas in the PCGTAW, heat input (Eqs. 1, 2) was computed from mean current (I_m).

$$I_m = \frac{I_p \times t_p + I_b \times t_b}{t_p + t_b} \text{ amps.} \tag{1}$$

Heat input (H.I.) was computed by using equation (ii),

$$HI = \eta \times \frac{I_m \times V}{S} \left(\frac{J}{\text{mm}} \right) \tag{2}$$

where S welding speed, mm/min; I_b background current, amps; I_p pulse current, amps; V voltage, V; t_p pulse current duration, ms; t_b background current duration, ms; η efficiency of the welding process; For the CCGTAW and PCGTAW process, arc efficiency (η) was chosen as 70%.

2.3 Microstructural Characterization

The weldment microstructures were assessed through an optical microscope (ZEISS) and scanning electron microscope (ZEISS). The assessment was performed at fusion zone, base metal, and heat-affected zone (HAZ). The specimens were extracted using an unconventional machining process (wire cut electrical discharge machine) in the direction perpendicular to the weldment. Figure 2 shows the specimens extracted for various characterization techniques. The microstructure specimens were polished

Table 1 Elemental composition of base metal and filler rods (wt %)

Element	Fe	Ni	Cr	Cu	Mo	Nb	Mn	Si	P	Al	C	Ti	S	W	Co
Incoloy 20	Bal	33.42	19.06	3.18	1.97	0.428	0.463	0.315	0.033	0.022	0.02	0.012	0.001	–	–
ERNiCrMo-2	14.80	Bal	20.38	–	9.22	0.36	0.42	0.50	–	0.12	0.05	–	–	0.76	0.50
ERNiCrMo-3	1.00	Bal	22.00	0.50	10.00	4.50	0.50	0.50	–	0.40	0.10	0.40	0.015	–	–

Fig. 1 Welded plates of Incoloy 20

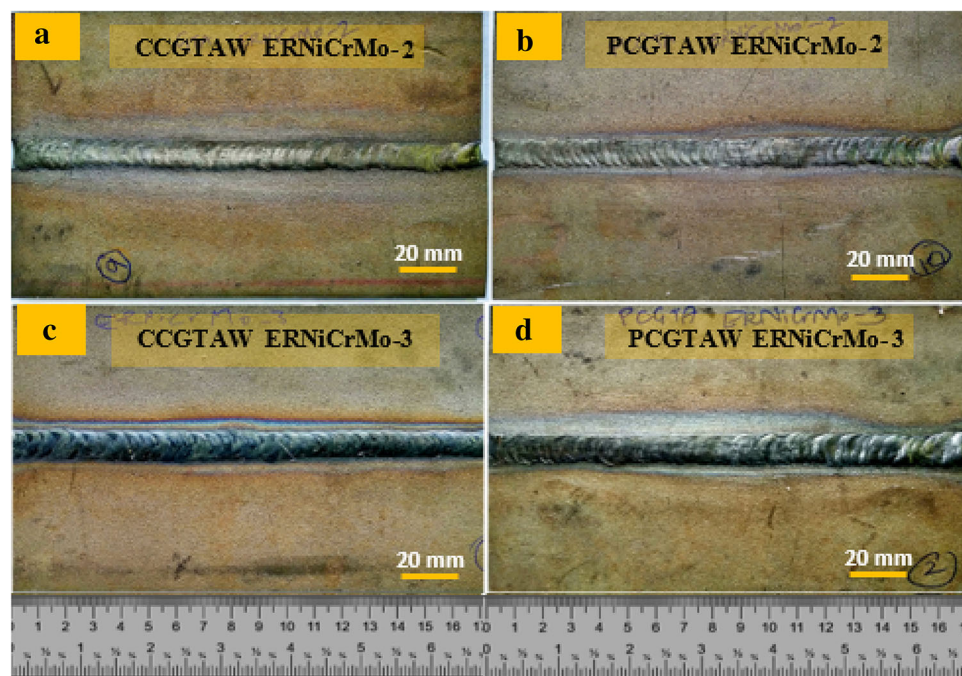


Table 2 Process parameters used for CCGTA welding of Incoloy20

Filler rod	Pass	Current (A)	Voltage (V)	Welding speed (mm/s)	Heat input (J/mm)	Total heat input (J/mm)
ERNiCrMo-2	Root	131	10.2	0.82	1145.5	2354
	First	131	10.2	1.84	508.38	
	Second	131	10.2	1.34	699.85	
ERNiCrMo-3	Root	131	9.7	0.88	1010.9	2179
	First	131	9.7	1.25	712.64	
	Second	131	9.7	1.95	455.21	

Table 3 Process parameters used for PCGTA welding of Incoloy 20

Filler rod	Pass	Pulse current, I_p (A)	Background current, I_b (A)	Voltage (V)	Pulse frequency (Hz)	% on time of peak current	Welding speed (mm/s)	Heat input (J/mm)	Total heat input (J/mm)
ERNiCrMo-2	Root	130	88	10.4	6	50	0.841	944	2283
	First	130	88	10.4	6	50	1.185	669	
	Second	130	88	10.4	6	50	1.185	669	
ERNiCrMo-3	Root	130	88	9.2	6	50	0.798	880	2039
	First	130	88	9.2	6	50	1.156	607	
	Second	130	88	9.2	6	50	1.271	552	

with SiC emery sheets utilized in the range of lower grade (220 grit) to a higher grade (2000 grit), followed by 0.5 μm alumina powder and ended with water polish to obtain mirror finish. Polished specimens were etched with electrolytic etching (12 V DC for 10 s) with oxalic acid in the volume ratio of 10% with deionized water on the fused

specimens to exhibit the microstructure of the base metal, HAZ, and fusion zone. Energy-dispersive X-ray spectroscopy (EDS) point analysis and line mapping were conducted on the weldments of the interdendritic region and dendritic core to examine the elemental segregation. X-ray diffraction analysis (XRD) was conducted on the

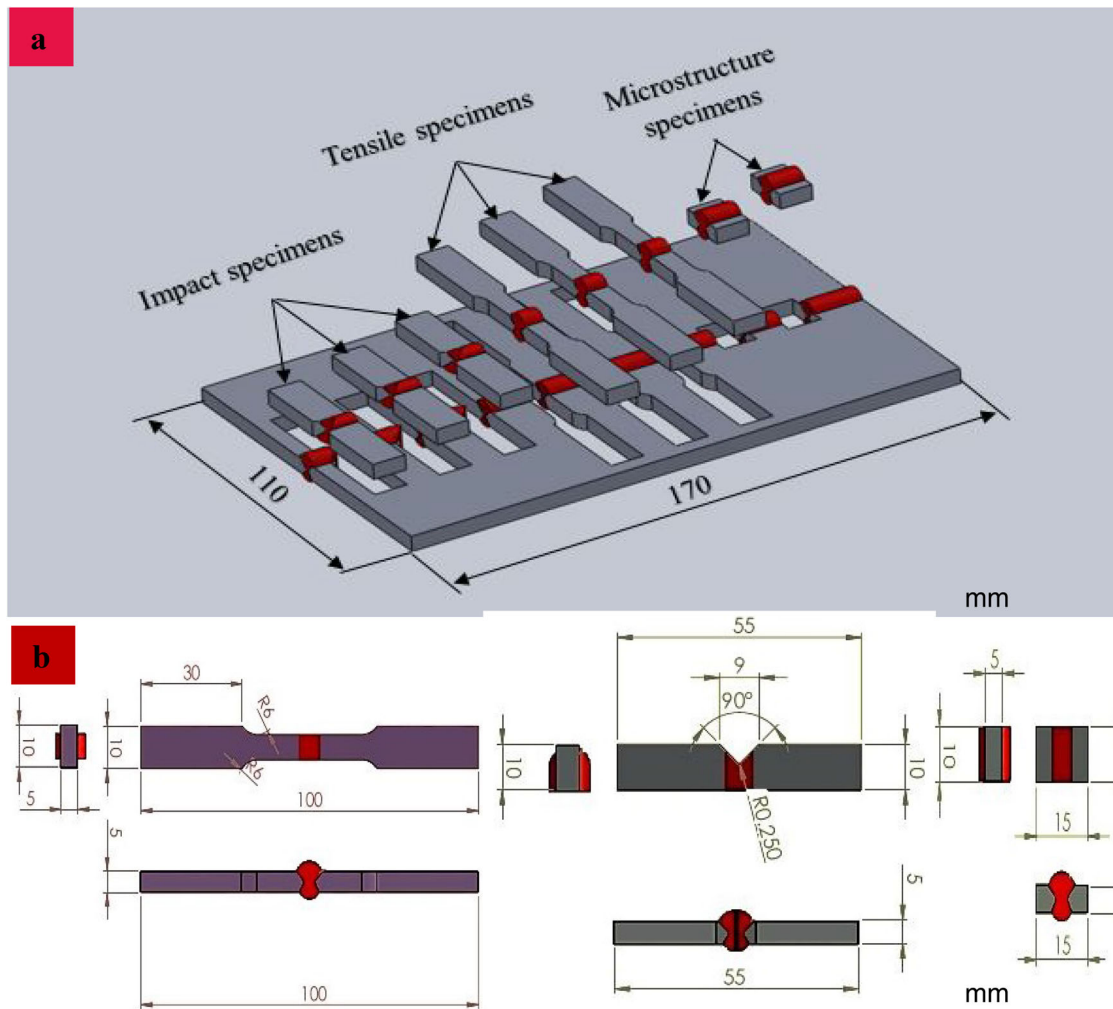


Fig. 2 a Layout of test coupons extracted for characterization, b extracted specimens with dimensions

weldments to assess the formation of intermetallic phases. Electron backscatter diffraction (EBSD) analysis was performed to examine the grain boundary characterization in the heat-affected zone.

2.4 Mechanical Characterization

Tensile strength (ultimate tensile strength, yield strength, and ductility) of the weldments and base metal were assessed using Instron make 8801 modes universal tensile machine (strain rate of 2 mm/min at ambient temperature). The weldments were cut as per the standard of ASTM [E8/E8M-16a (sub-size)]. The toughness of the base metal and weldments was evaluated using the Charpy test (V-notch) at ambient temperature. The test specimens were prepared as per the standard of ASTM E23. V-notch was made in the center of the weldments. Three samples were evaluated for both tests to verify the reproducibility of the outcomes. Further,

fractography was conducted through the SEM to evaluate the mode of failures. Vickers microhardness test was conducted on the weldments. The applied load was 500gf with a dwell time of 10 s. The test was performed within an interval of 0.25 mm between two points.

2.5 Electrochemical Corrosion Test

Electrochemical corrosion properties of Incoloy 20 weldments (dimension: 10 × 10 × 5 mm) were examined using potentiodynamic polarization test (temperature: 24 °C and NaCl solution: 3.5%). Incoloy 20 is widely used in applications such as seawater heat exchanger and pressure vessels. Hence, sodium chloride (NaCl) environment is chosen for the present study. The test was conducted as per standard (ASTM G61-86) using IVIUM electrochemical workstation. The workstation comprised of three electrodes, such as reference [saturated calomel electrode (SCE)], counter (platinum electrode), and working

(sample) electrodes. At the start, the delay (10 s) was provided to generate an open circuit potential (OCP) with a duration of 1800 s for all the samples. Tafel plot was computed between the values of -1 v/SCE to +1 v/SCE for all the samples with the scan rate of 10 mV/s. The required parameters were computed from the IVIUM software, and corrosion rate of all the samples was computed through equation (iii):

$$\text{Corrosion rate} = 0.13 \times I_{\text{corr}} \times E.W./A \times d \quad (3)$$

where I_{corr} is the corrosion current density; A , area in cm^2 ; $E.W.$, the equivalent weight of the sample utilized in (g/eq); and density (in g/cm^3).

The equivalent weight of Incoloy 20 was computed, that was 25.4 g/eq and density of 8.08 g/cm^3 . Similarly, the equivalent weight of ERNiCrMo-2 (27.92 g/eq) and ERNiCrMo-3 (25.573 g/eq) filler wires were found per the ASTM G 102-89 standard and density of filler wires were 8.22 g/cm^3 and 8.44 g/cm^3 , respectively.

3 Results and Discussion

3.1 Macrostructures of weldments

Macrostructures of Incoloy 20 weldments are captured and evaluated to find the defects in the welds (Fig. 3a–d). It is confirmed that no defects are seen from the macroscopic examination. Good welding morphology is seen from Fig. 3, which also denoted steady fluid flow in the weld pool. Weld pool morphology of CCGTAW and PCGTAW specimens shows the effects of the buoyancy force and surface tension in the shape and size of the weld bead profile. The reduced buoyancy force in PCGTAW provides

proper filling of molten metal along with the groove profile as well as a reduction in the weld bead width. Width of the WZ for both filler metals is less and narrow for PCGTAW specimens as compared to CCGTAW specimens. Low shear stress instigated by surface tension in PCGTAW also reduces the weld bead width due to the decreased flow of molten metal from the weld center to the weld interface [18]. It is evinced that process parameters utilized in this work are optimum to produce Incoloy 20 plates with two different filler wires.

3.2 Microstructures of Incoloy 20 Weldments

3.2.1 Base Metal Microstructure

The microstructure of as-received hot-rolled and solution-annealed Incoloy 20 is captured as shown in Fig. 4a, b. Incoloy 20 microstructure reveals the fine equiaxed grains, which improve the toughness and corrosion properties.

3.2.2 CCGTAW and PCGTAW with ERNiCrMo-2 and ERNiCrMo-3 Filler Wires

Microstructures of Incoloy 20 weldment with ERNiCrMo-2 using CCGTAW and PCGTAW are shown in Fig. 5a–d. Microstructures of ERNiCrMo-3 weldments are shown in Fig. 6a–d. Microstructures show columnar and cellular structures in the weldments of Incoloy 20 with CCGTAW specimens of both fillers. The coarse microstructure at HAZ in the CCGTAW specimens is produced due to higher heat input [ERNiCrMo-2 (2354 J/mm) ERNiCrMo-3 (2179 J/mm)] and slower cooling rate during solidification. Columnar and cellular dendrites formation could be explained through the solidification procedure that changes

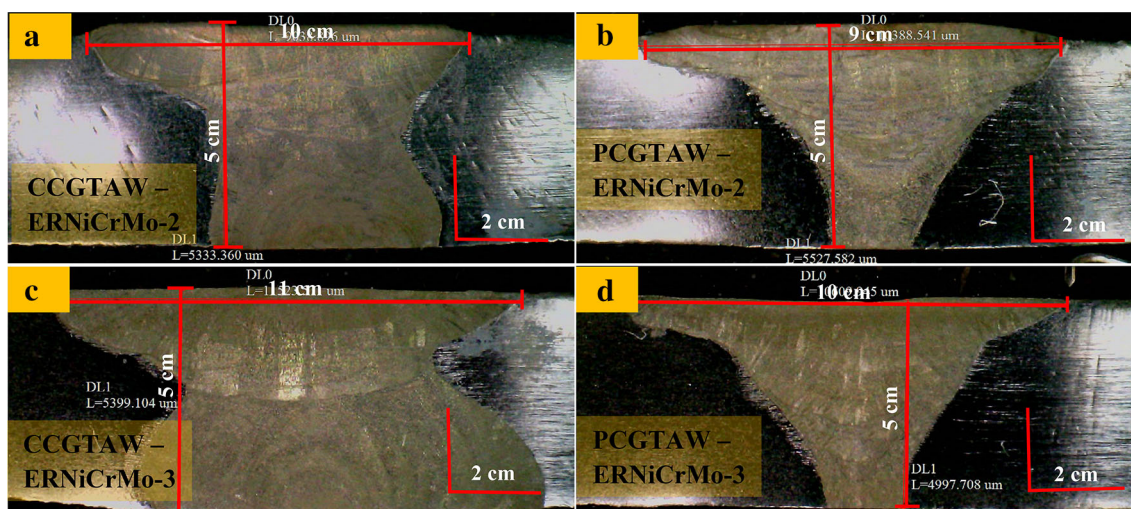


Fig. 3 Macrostructures of Incoloy 20 weldment with ERNiCrMo-2 using **a** CCGTAW, **b** PCGTAW and with ERNiCrMo-3 using, **c** CCGTAW, **d** PCGTAW

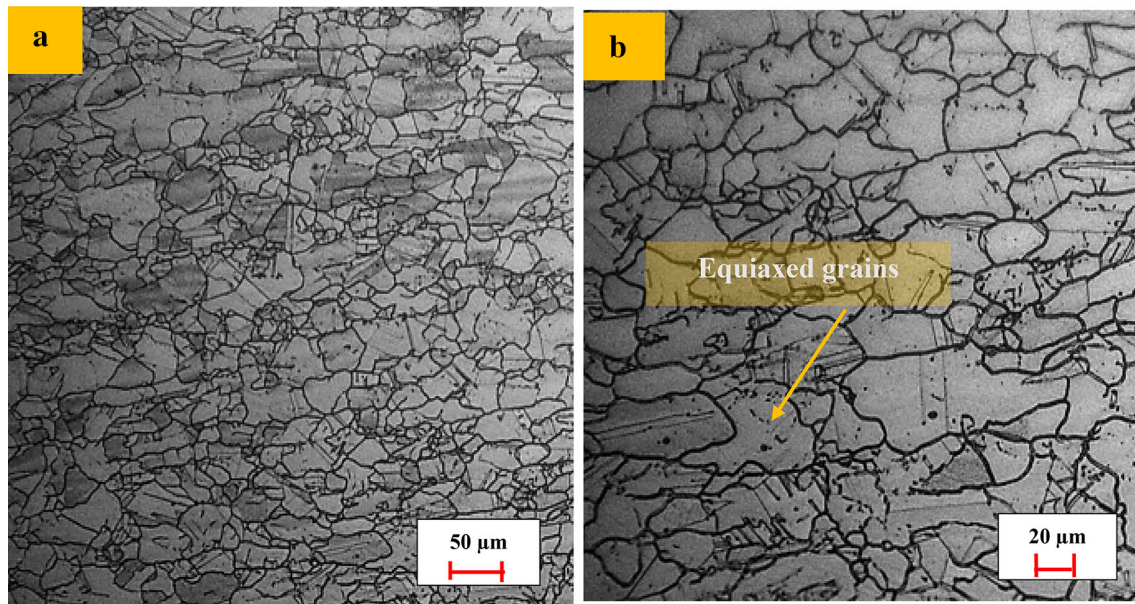


Fig. 4 Microstructures of as-received Incoloy 20 **a** 100 \times , **b** 200 \times

with thermal gradient resulting in disintegration in the planar solid–liquid interface. In common, a lower thermal gradient yields enormous grain growth in the weld center. Besides, steep temperature gradient results in lesser grain growth nearer to the fusion line. Grain growth in the easy growth directions ($\langle 100 \rangle$ crystallographic plane) matching with the heat dissipation direction (perpendicular to weld pool) is the reason for the formation of columnar structure nearer to the fusion line.

PCGTAW specimens with both filler wires are observed with equiaxed grain structures in the weld center. Equiaxed structures in the PCGTAW specimens are formed due to low heat input [ERNiCrMo-2 (2283 J/mm) and ERNiCrMo-3 (2039 J/mm)] during fusion welding process with the rapid rate of solidification. In the PCGTAW specimens, pulsing current at the stage of welding results in refinement of microstructure. Commonly, thermal fluctuation in the weld pool created through the cyclic shift of input energy causes periodic pauses in the solidification process. New grains are produced in the weldment during peak current (metal melting takes place) and base current (solidification takes place). In the following cycle, the increase in the current leads to the hindrance of new grains formation and the occurrence of growing grains re-melting. Repetition of these cycles leads to variation in the shape and size of the weld pool and favorable new grain growth occur due to temperature fluctuation in the weld pool. Hence, refinement of the microstructure is produced due to an increment of grain growth rate within a small distance that allows in the growth of more grains. Refined microstructures are well matched with other literature reported earlier [11, 16–18]. Figures 5a, c, and 6a, c show

microstructures of HAZ of CCGTAW and PCGTAW specimens. The refined grain structure at the HAZ is observed in the PCGTAW specimens when compared with CCGTAW specimens. Lower and narrower heat input supplied in PCGTAW causes the refinement of grains.

3.3 SEM/EDS Analysis of Incoloy 20 Weldments

SEM results of Incoloy 20 welded with ERNiCrMo-2 and ERNiCrMo-3 filler wires are shown in Figs. 7, 8, 9, 10, 11, 12, 13 and 14. SEM images of Incoloy 20 weldments (weld interface and weld center) are observed with precipitates. It is observed that precipitates are produced as tiny particles in the interdendritic regions, which is formed at the end of solidification. Various dendritic structures such as columnar, cellular, and equiaxed dendrites are also noticed in the SEM analysis.

EDS analysis evaluates elemental segregation of the weldments at the dendritic core and interdendritic regions are given as shown in Figs. 7, 8, 9, 10, 11, 12, 13 and 14. The main issue in the Fe–Ni–Cr system is hot fissuring due to the segregation of Nb, Ti, and Si elements [19]. In this investigation, elements such as Fe, Ni, Cr, Mo, W, Nb, Ti, and Si are emphasized for evaluation of elemental segregation.

Segregation of Si and Mo elements is found at the interdendritic region of the weld interface [Fig. 7a (i), (ii)] and weld center [Fig. 7b (i), (ii)] of CCGTAW ERNiCrMo-2 weldment. The line mapping also confirms similar segregation as shown in Fig. 8.

Molybdenum and tungsten are segregated at the interdendritic regions of the weld interface [Fig. 9a (i), (ii)] and

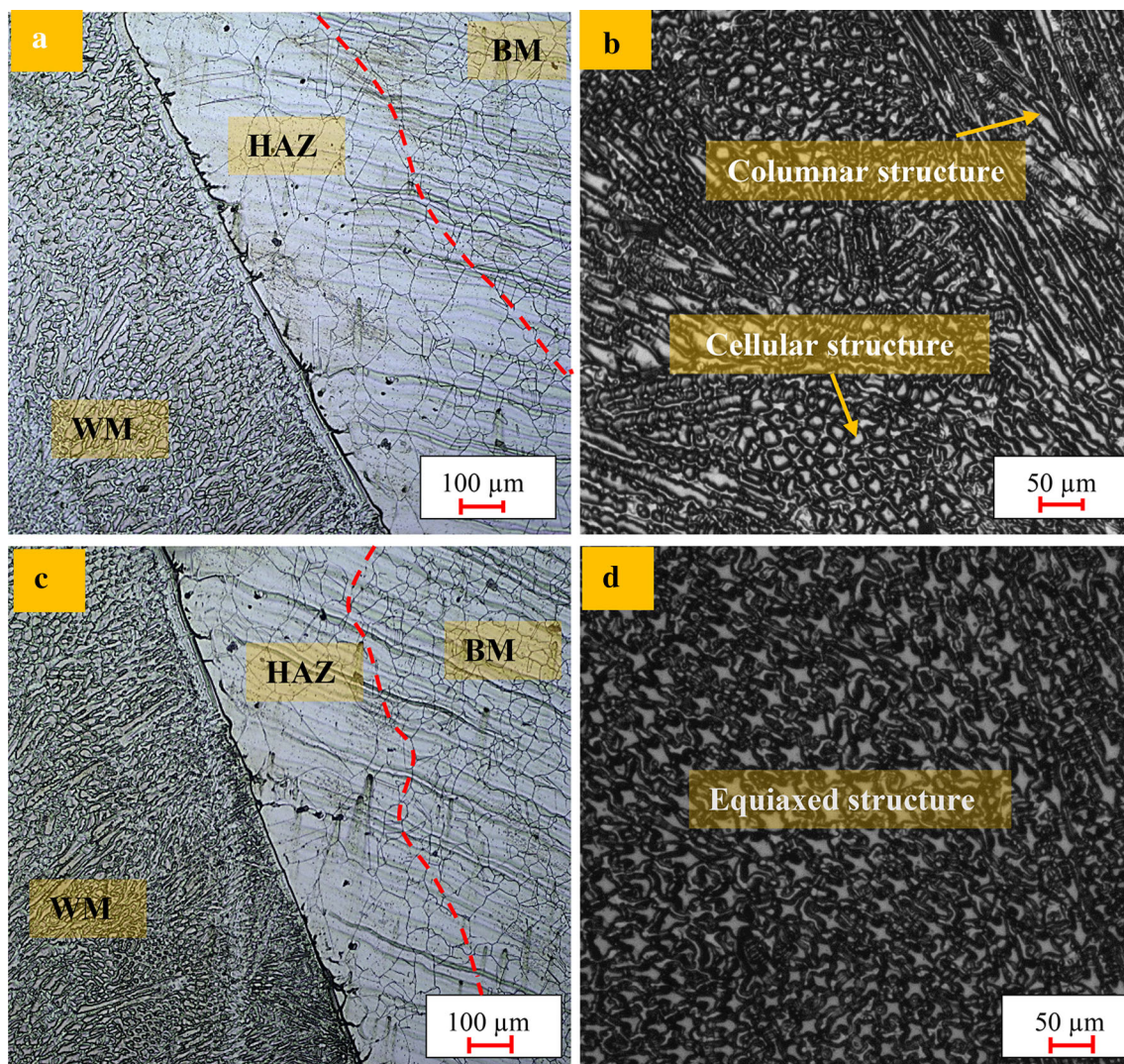


Fig. 5 Microstructures of Incoloy 20 welds with ERNiCrMo-2 using CCGTAW **a** weld interface, **b** weld center and PCGTAW, **c** weld interface, **d** Weld center

weld center [Fig. 9b (i), (ii)] of PCGTAW ERNiCrMo-2 weldment. Line mapping also confirms similar segregation of the precipitates, as shown in Fig. 10.

Segregation of Nb and Mo elements is noticed at the interdendritic regions of the weld interface [Fig. 11a (i), (ii)] and weld center [Fig. 11b (i), (ii)] of CCGTAW ERNiCrMo-3 weldment. Line mapping also confirms the similar segregation of the precipitates as shown in Fig. 12.

Reduced segregation of Nb and Mo elements is found at the interdendritic regions of the weld interface [Fig. 13a (i), (ii)] and weld center [Fig. 13b (i), (ii)] of PCGTAW ERNiCrMo-3 weldment. Line mapping also confirms similar segregation of the precipitates (Fig. 14).

In this study, segregation of major elements such as Mo, W, Si, and Nb is noticed. Segregation of Mo and W elements is noticed due to the atomic radius difference

between the matrix (Ni) and alloying elements (Mo and W), where the differences are 9% and 10% [17]. Solid solution strengthening (γ and γ') is offered through the Mo and W elements in the nickel-based alloys. Silicon is the eutectic constituent element that is the reason for the segregation in the precipitation strengthened alloy [1]. The hot cracking tendency is observed with silicon segregation in the Incoloy 800 weldments, and segregation of Si (1.25 wt%) also leads to hot cracking in the nickel-based alloys [20]. Even though segregation of silicon occurs in the ERNiCrMo-2 weldments, still, hot cracking is not observed due to the silicon weight percentage (within the range of 0.2–0.8%). Similar results were discussed previously for the silicon segregation [19]. Niobium segregation could be attributed to the amount of Nb (γ' and γ'' promoting element) in the filler wire ERNiCrMo-3. Even though segregation of Nb occurs, still, hot cracking is not

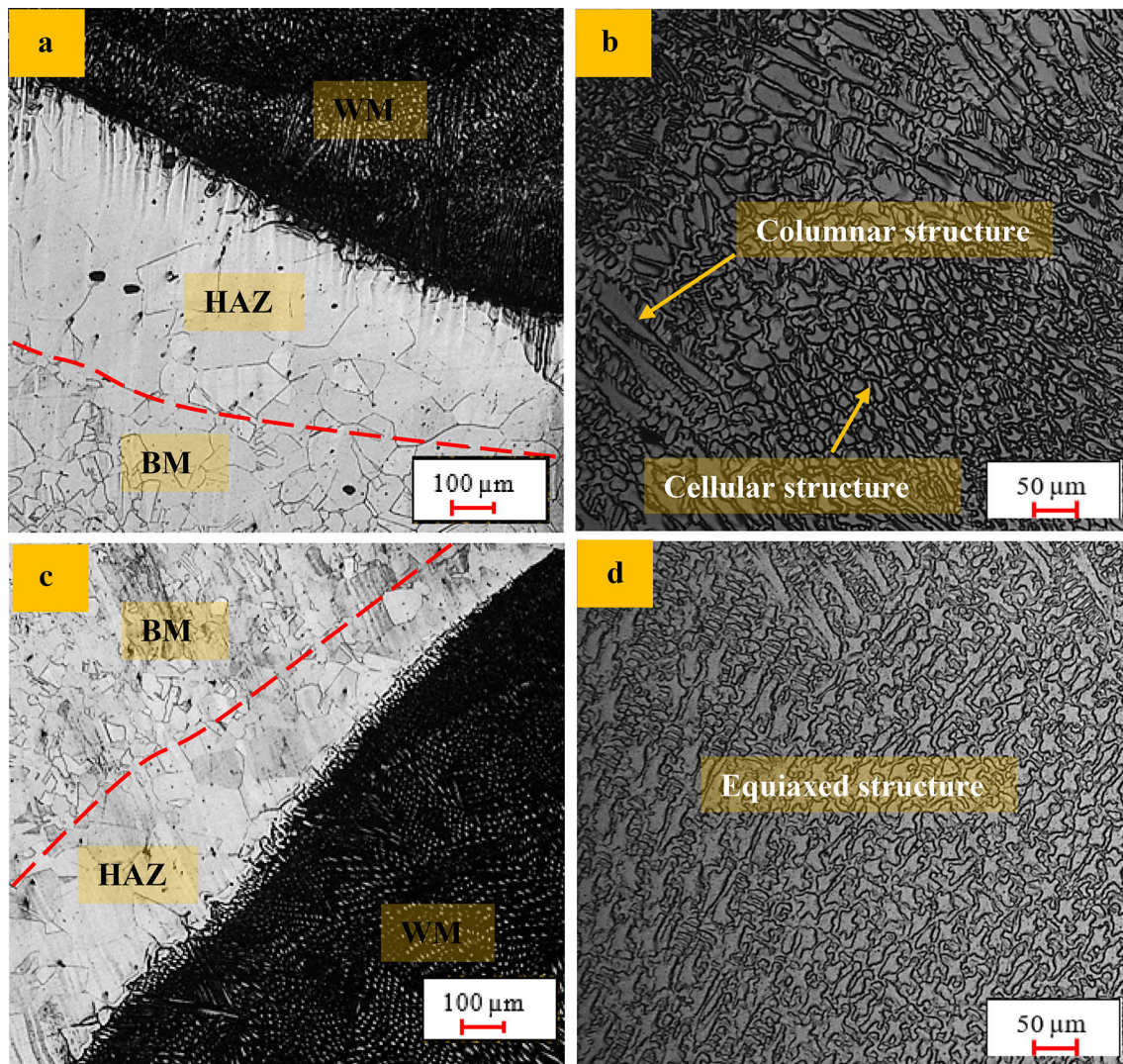


Fig. 6 Microstructures of Incoloy 20 welds with ERNiCrMo-3 using CCGTAW **a** weld interface, **b** weld center and PCGTAW, **c** weld interface, **d** weld center

observed in this investigation, because the hot cracking tendency is seen with combined segregation of Si and Ti with the little amount of Nb as reported earlier [19]. The pulsed current mode of weldments shows lesser segregation as compared to continuous mode current due to constitutional supercooling.

3.4 XRD Analysis of Incoloy 20 Weldments

XRD results are exhibited for Incoloy 20 weldments with ERNiCrMo-2 and ERNiCrMo-3 filler wires using CCGTAW and PCGTAW processes, as shown in Figs. 15, 16, 17 and 18. A huge volume of segregated phases in the CCGTAW specimens is denoted by using the higher peak intensity of XRD plots. It is concluded that the deviation in the peak intensity occurs due to high heat input and slow cooling rate in the CCGTAW specimens. In this work, the

peak intensity of PCGTAW specimens is lesser than that of CCGTAW specimens.

XRD result of CCGTAW ERNiCrMo-2 weldment (Fig. 15) is noticed with interstitial compounds such as $M_{23}C_6$ ($Mo_{23}C_6$), MC (MoC), and $M_{12}C$ ($Si_{12}C$) due to γ -elements such as Fe, Cr, and Mo and γ' -elements such as Mo and Si. XRD result of PCGTAW ERNiCrMo-2 weldment (Fig. 16) is found with interstitial compounds such as $M_{23}C_6$ ($Mo_{23}C_6$) and MC (MoC) due to γ -elements (Fe, Cr, W, and Mo) and γ' -elements (Mo).

XRD result of CCGTAW ERNiCrMo-3 weldment (Fig. 17) is noticed with interstitial compounds such as $M_{23}C_6$ ($Mo_{23}C_6$) and MC (MoC and NbC) and intermetallic compound (Ni_8Nb) due to γ -elements such as Fe, Cr, and Mo and γ' -elements such as Mo and Nb. XRD result of PCGTAW ERNiCrMo-3 weldment (Fig. 18) is found with interstitial compounds such as $M_{23}C_6$ ($Mo_{23}C_6$)

Fig. 7 SEM/EDS analysis of CCGTAW ERNiCrMo-2 sample **a** SEM - weld interface (i) EDS-dendritic core (ii) EDS-interdendritic region, **b** weld center (i) EDS-dendritic core (ii) EDS-interdendritic region

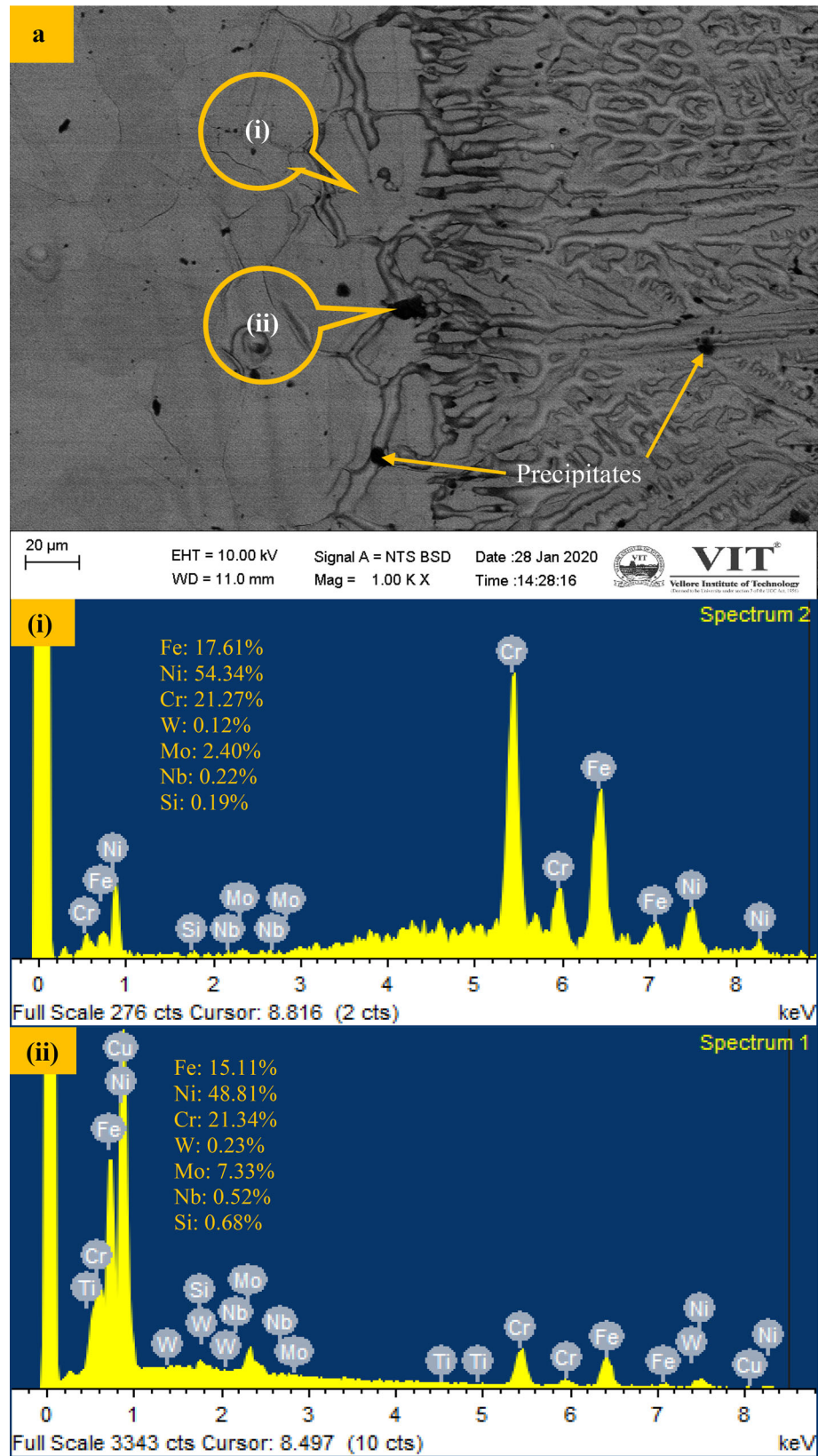
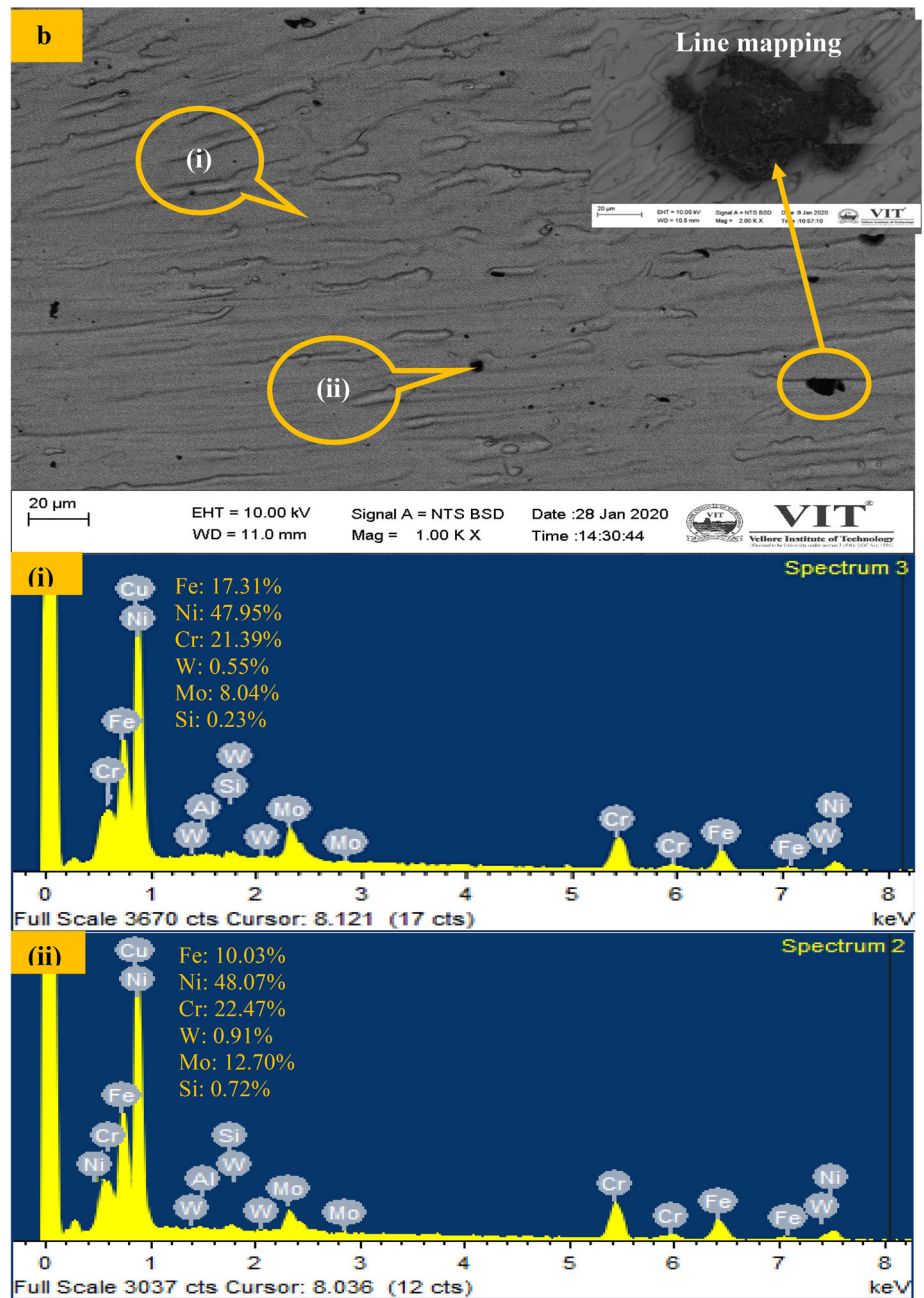


Fig. 7 continued



and MC (MoC and NbC) and intermetallic compound (Ni_8Nb) due to γ -elements (Fe, Cr, and Mo) and γ' -elements (Mo and Nb).

In the XRD analysis, interstitial compounds (M_{23}C_6 , M_{12}C , and MC) are found, which are similar to the previous literature [3, 21, 22], and intermetallic compound (Ni_8Nb) is observed as reported earlier [16]. Interstitial compounds formed as tiny particles at interdendritic regions offer higher mechanical properties, and these compounds formed as brittle-cellular form offer diminution of ductility [18]. The intermetallic compound is brittle in nature which reduces strength. In general, precipitation-

hardened alloys produce γ' precipitates at the final stage of solidification due to Mo, W, Nb, and Si elements.

3.5 Microhardness Test Results of Incoloy 20 Weldments

Microhardness results for Incoloy 20 weldments with ERNiCrMo-2 and ERNiCrMo-3 filler wires using CCGTAW and PCGTAW are shown in Fig. 19. Average hardness values (Table 4) of the base metal, CCGTAW ERNiCrMo-2, and PCGTAW ERNiCrMo-2 are 208 HV, 194 HV, and 206 HV, respectively. Table 4 lists the

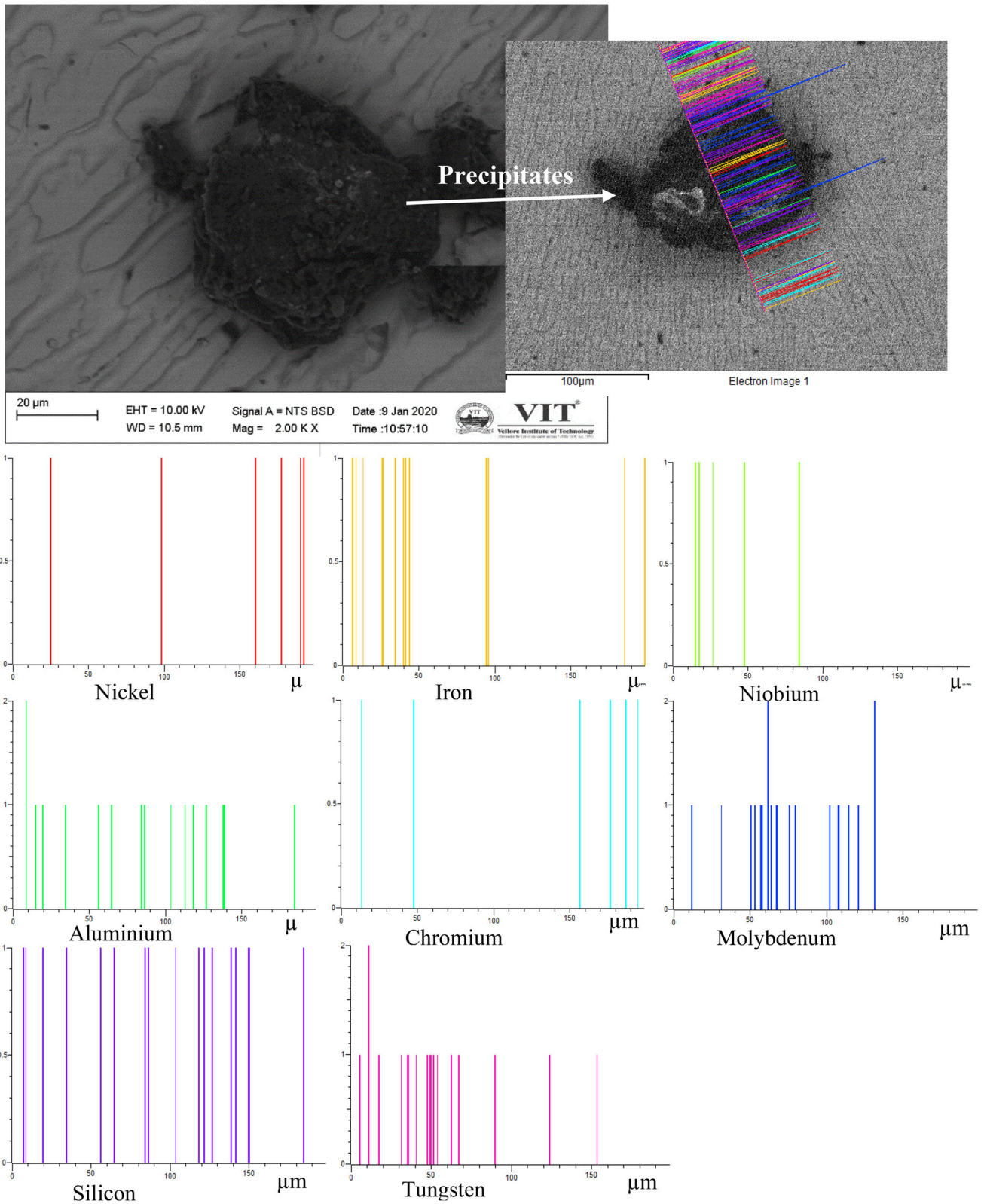


Fig. 8 Line mapping of a precipitate in CCGTAW ERNiCrMo-2 weldment

Fig. 9 SEM/EDS analysis of PCGTAW ERNiCrMo-2 sample
a SEM-weld interface (i) EDS-dendritic core (ii) EDS-interdendritic region, **b** weld center (i) EDS-dendritic core (ii) EDS-interdendritic region

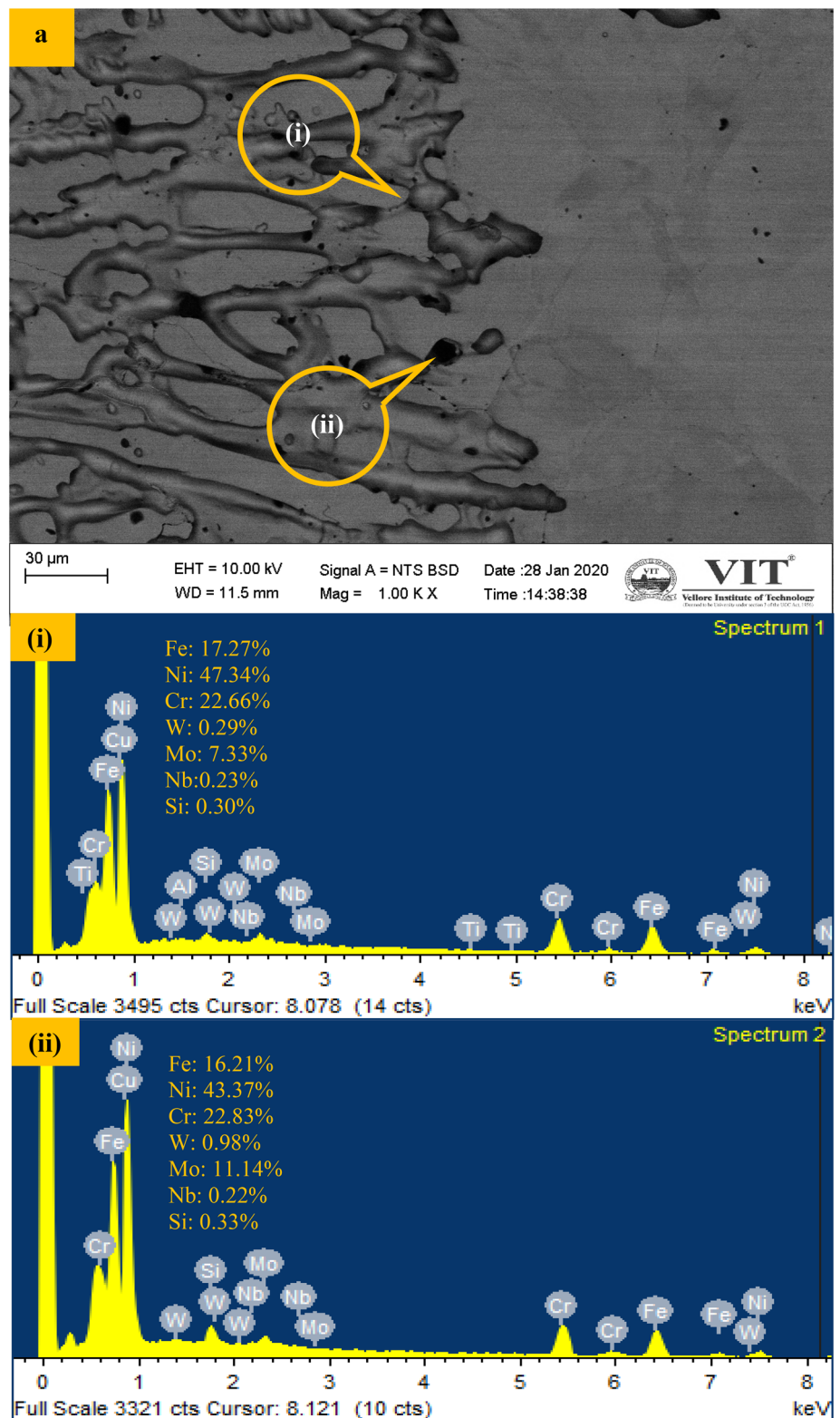
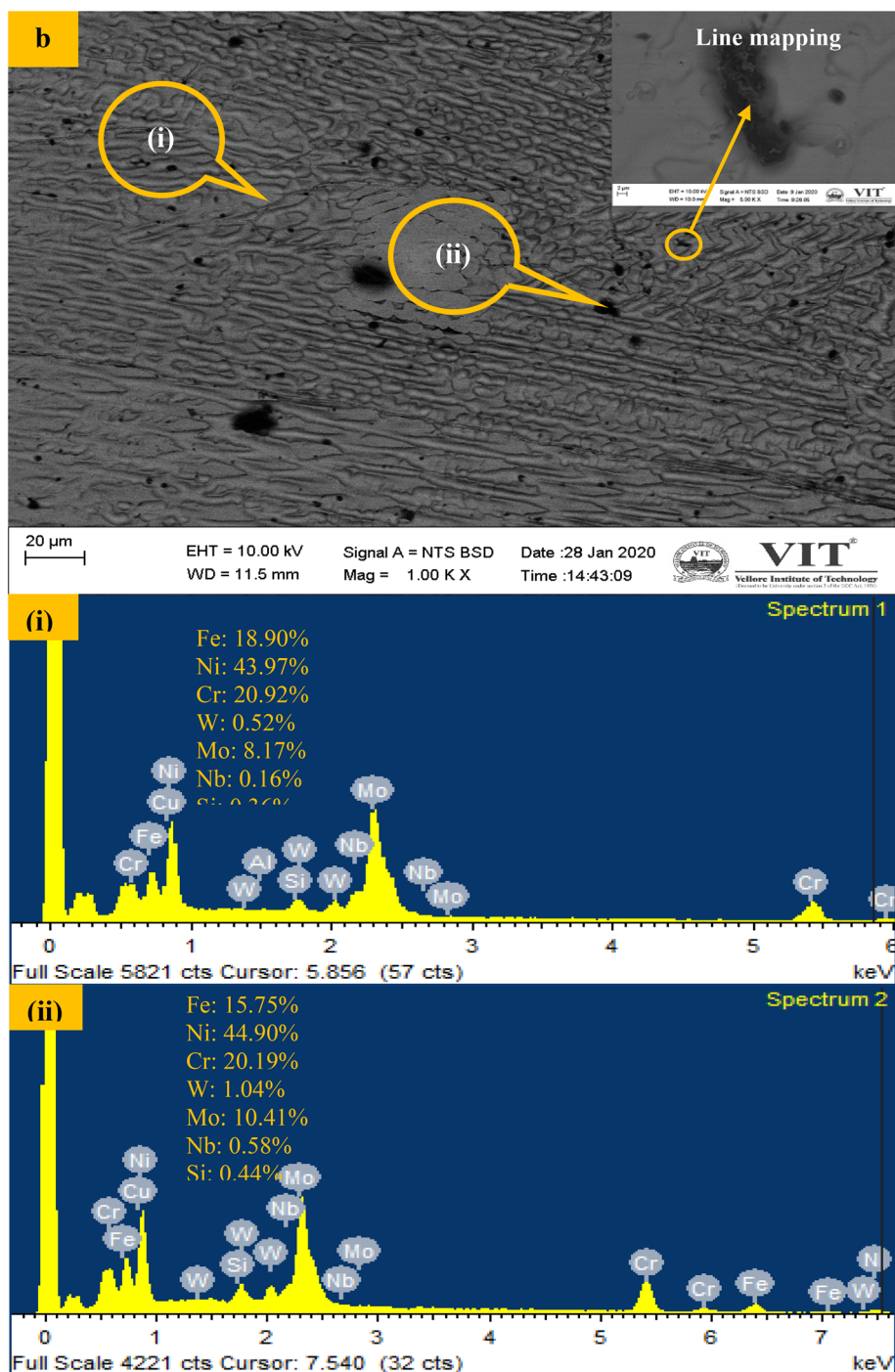


Fig. 9 continued



average hardness values of CCGTAW ERNiCrMo-3 (205 HV) and PCGTAW ERNiCrMo-3 (215 HV).

Weldments of CCGTAW and PCGTAW with ERNiCrMo-2 and ERNiCrMo-3 filler wires are found with lower hardness at HAZ. Lessening of hardness occurs due to grain coarsening in the HAZ. Similar observations are

discussed earlier for the Incoloy 800H [6]. PCGTAW weldments are found with marginally higher average hardness values while compared with CCGTAW weldments. Enhanced hardness values could be attributed to PCGTAW due to low heat input, which offers an equiaxed dendrite structure in comparison with CCGTAW. Little

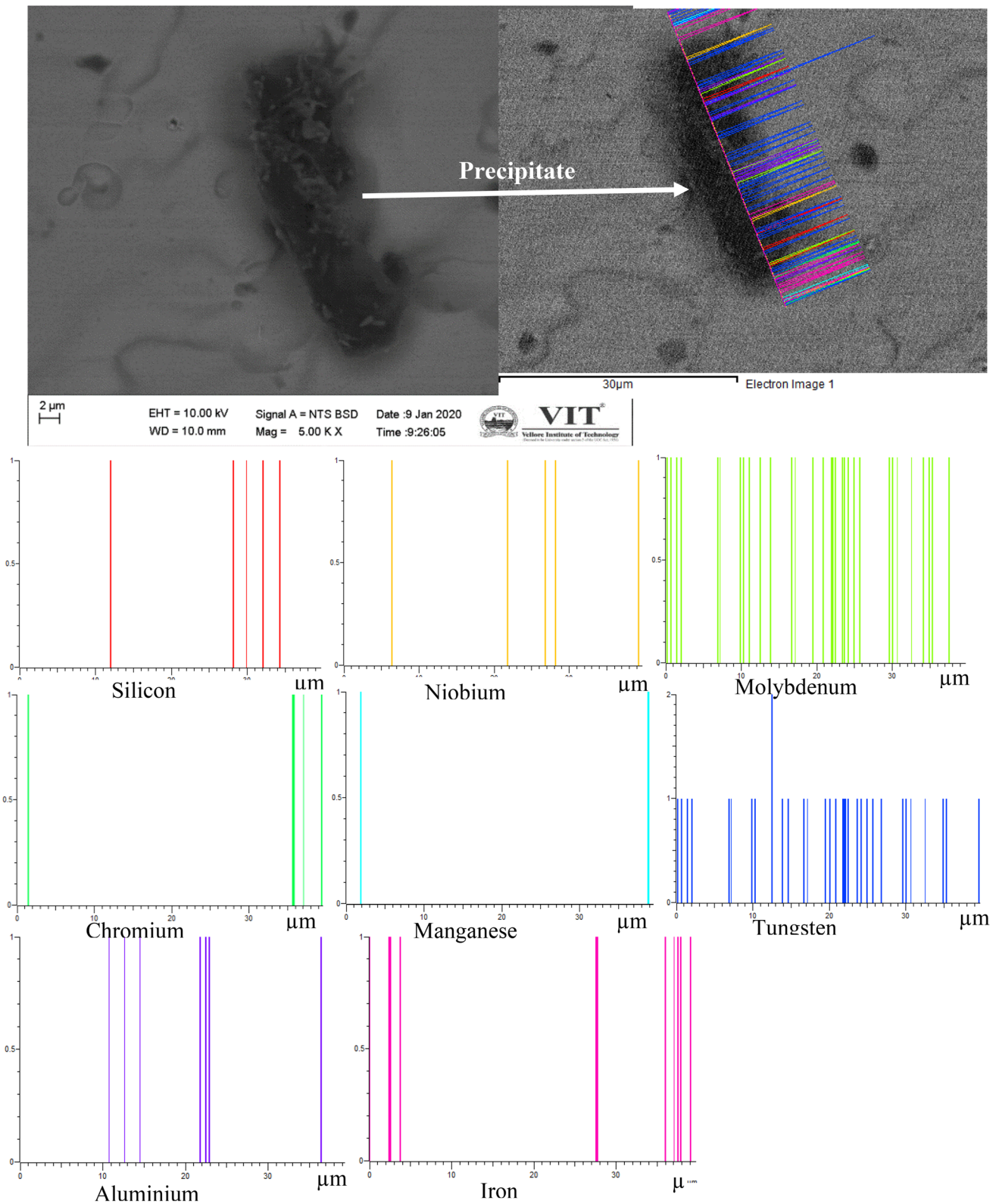


Fig. 10 Line mapping of a precipitate in PCGTAW ERNiCrMo-2 weldment

Fig. 11 SEM/EDS analysis of CCGTAW ERNiCrMo-3 sample **a** SEM-weld interface (i) EDS-dendritic core (ii) EDS-interdendritic region, **b** weld center (i) EDS-dendritic core (ii) EDS-interdendritic region

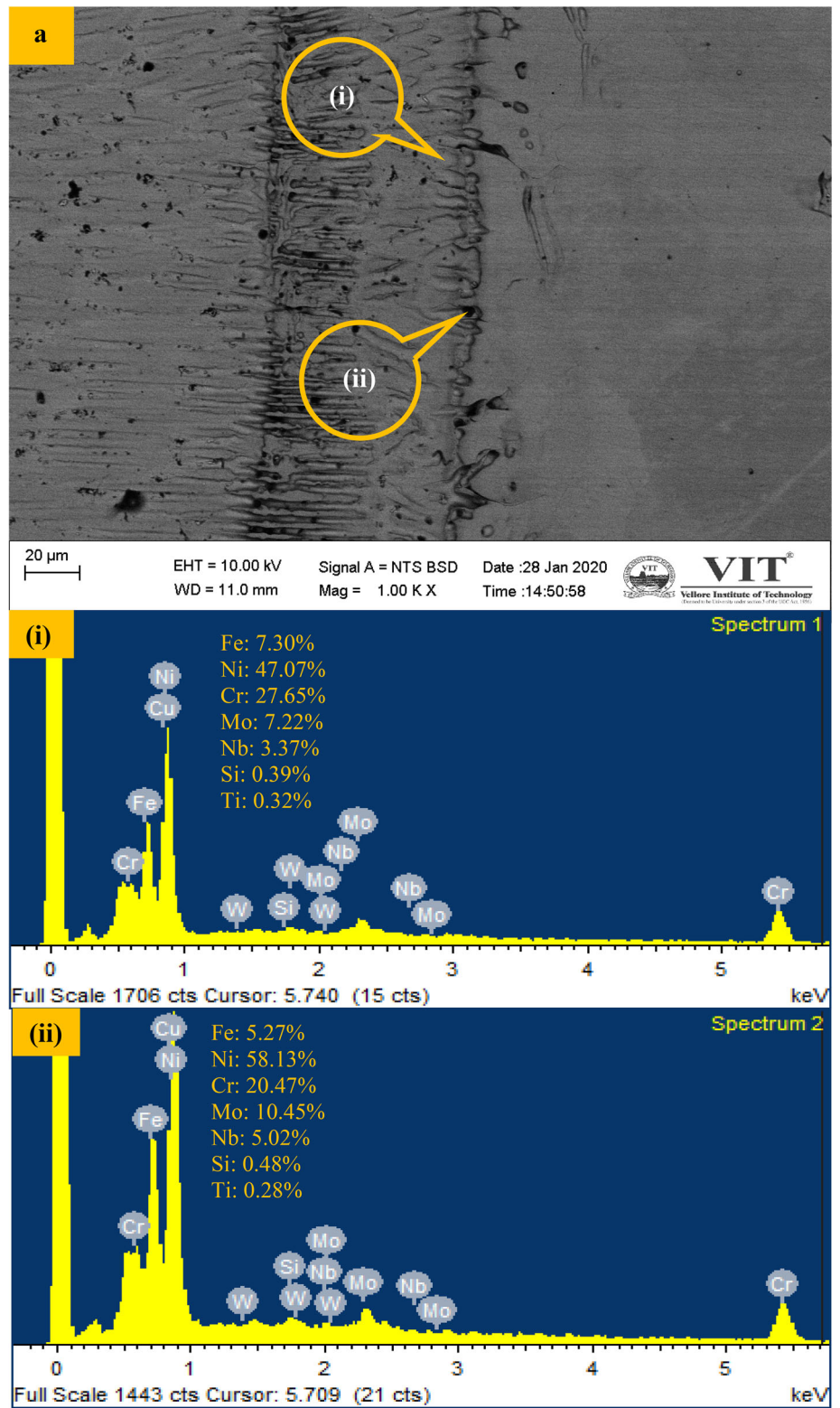
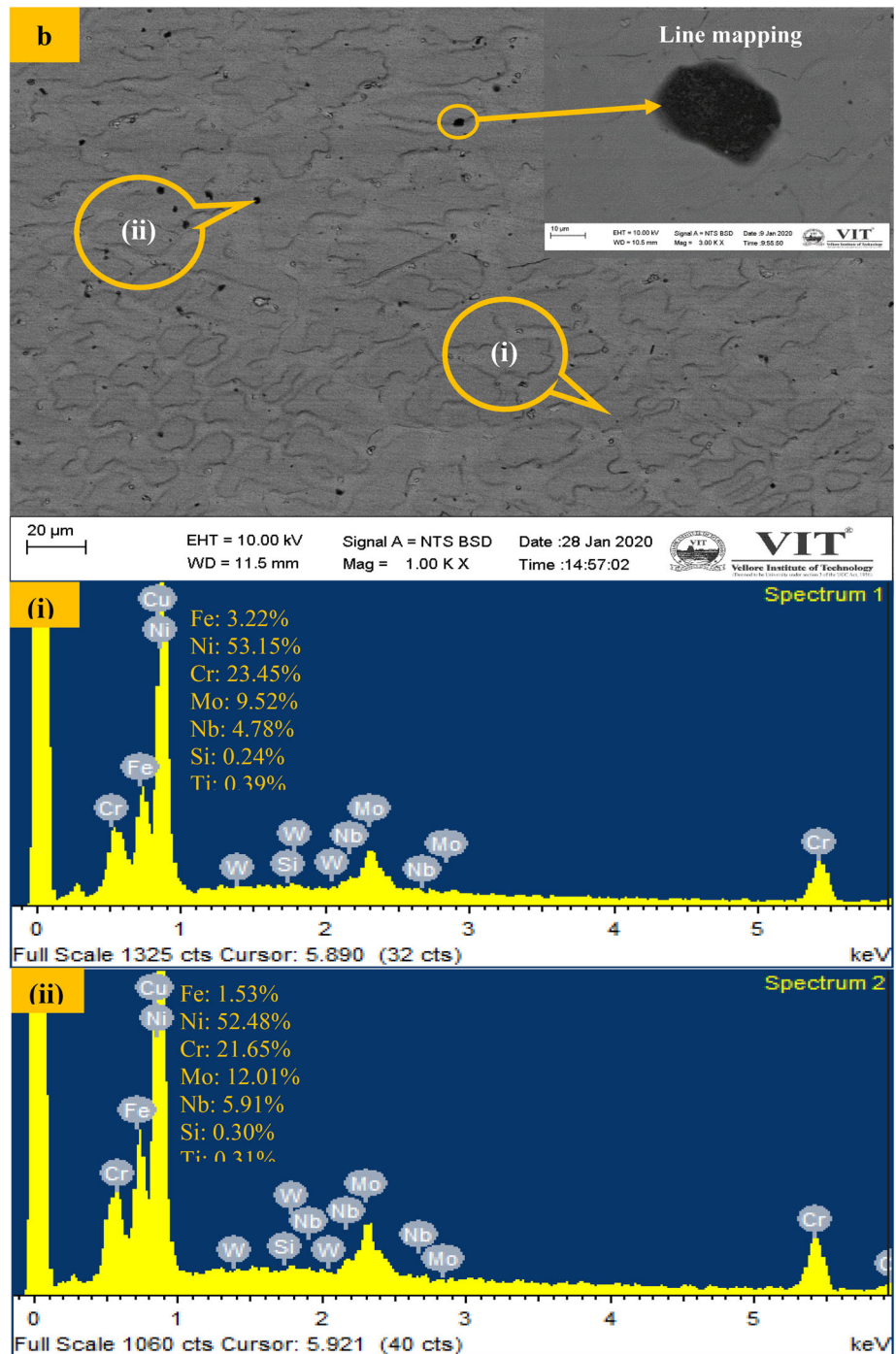


Fig. 11 continued



enhancement in the hardness of PCGTAW ERNiCrMo-2 is found due to W segregation at interdendritic regions. Weldments of ERNiCrMo-3 are noticed with little enhanced hardness due to intermetallic compound (Ni₃Nb). The differences in hardness are obtained in the weldments due to microstructural changes (columnar, cellular, and equiaxed dendrites) [1].

3.6 Impact Results of Incoloy 20 Weldments

The photograph of the impact test specimens is shown in Fig. 20. Impact tests examine toughness values for Incoloy 20 weldments with ERNiCrMo-2 and ERNiCrMo-3 filler wires using CCGTAW and PCGTAW processes that are listed in Table 4.

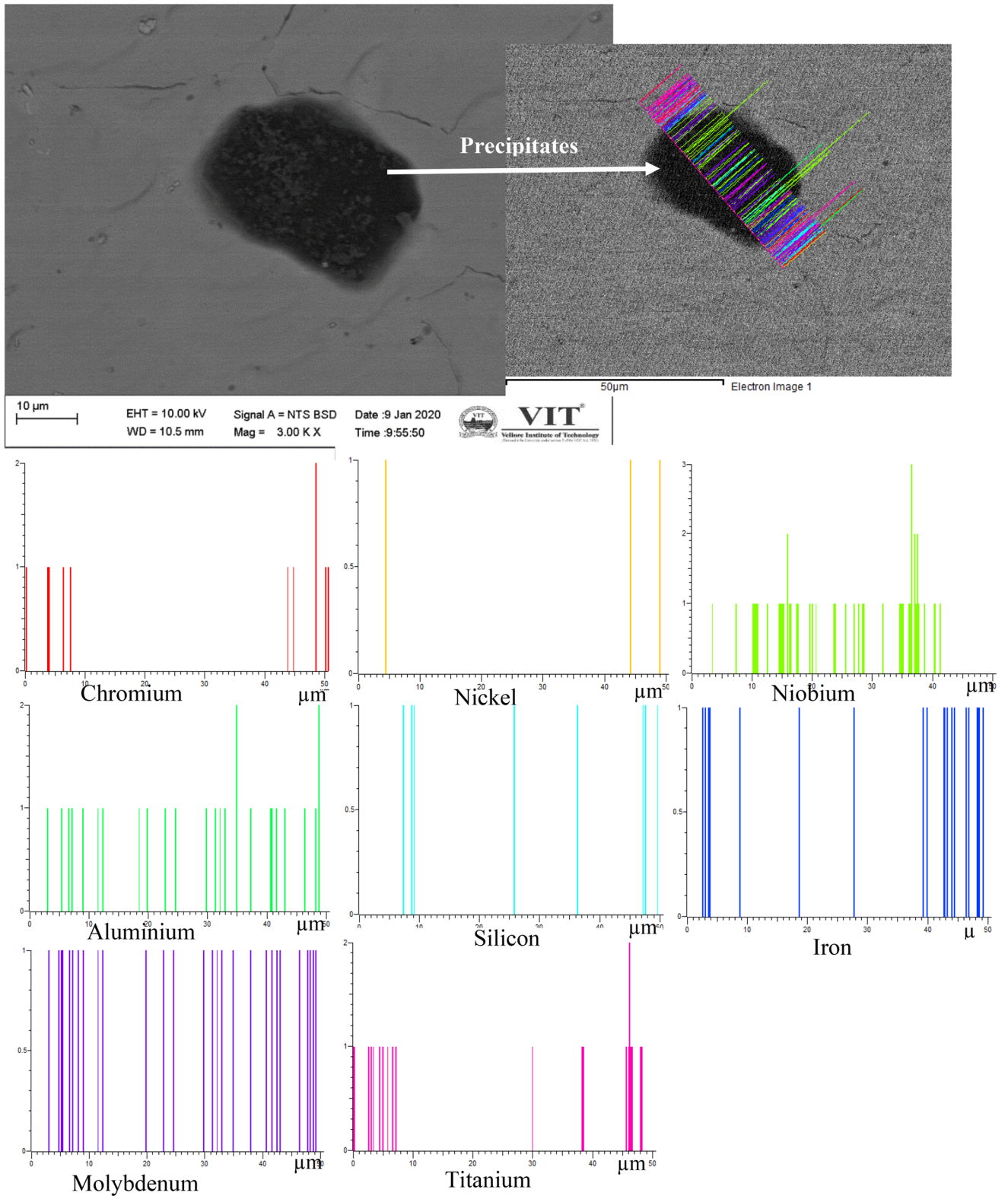


Fig. 12 Line mapping of a precipitate in CCGTAW ERNiCrMo-3 weldment

Fig. 13 SEM/EDS analysis of CCGTAW ERNiCrMo-3
 sample a) SEM - weld interface
 (i) EDS-dendritic core (ii) EDS-interdendritic region
 b) weld center
 (i) EDS-dendritic core
 (ii) EDS-interdendritic region

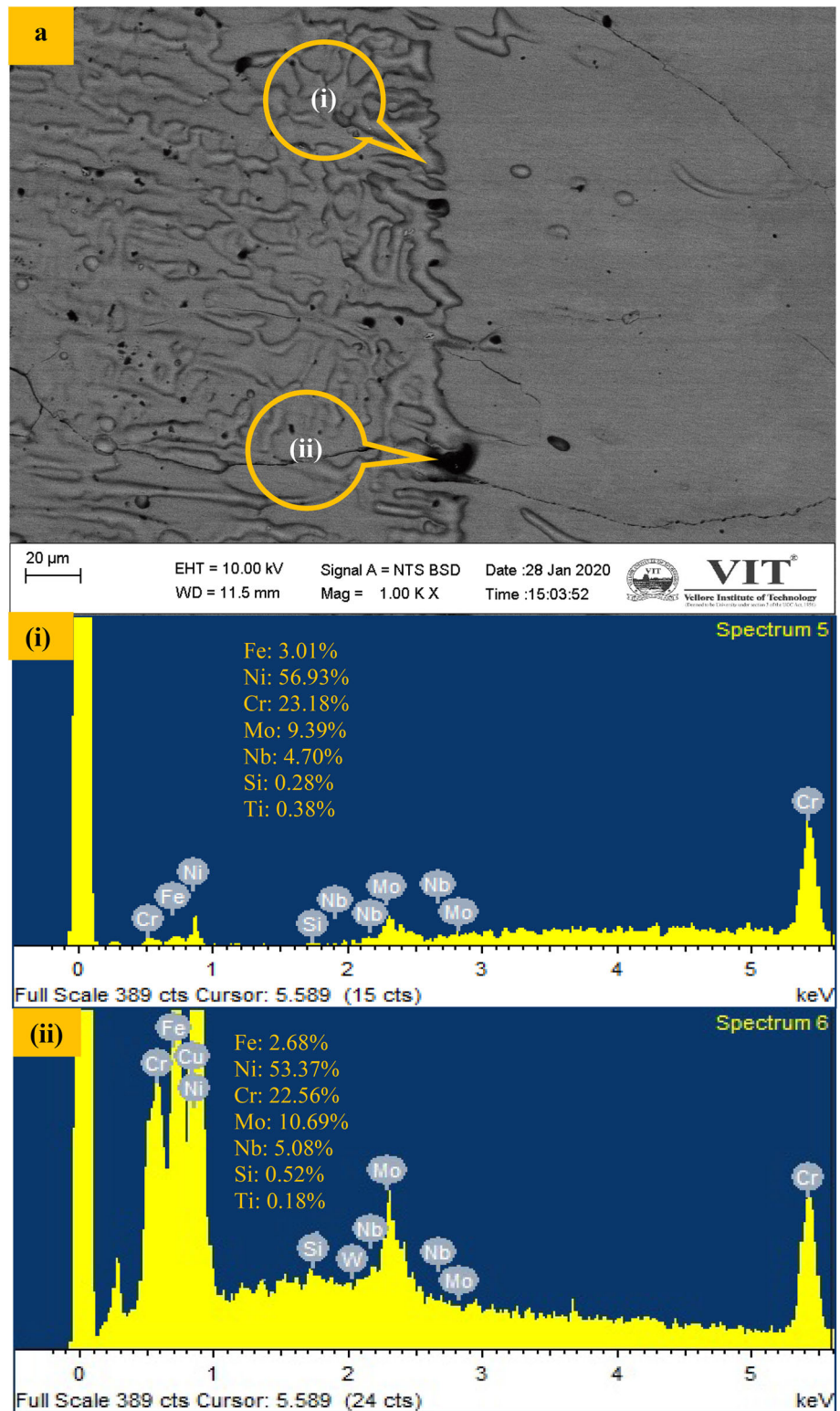
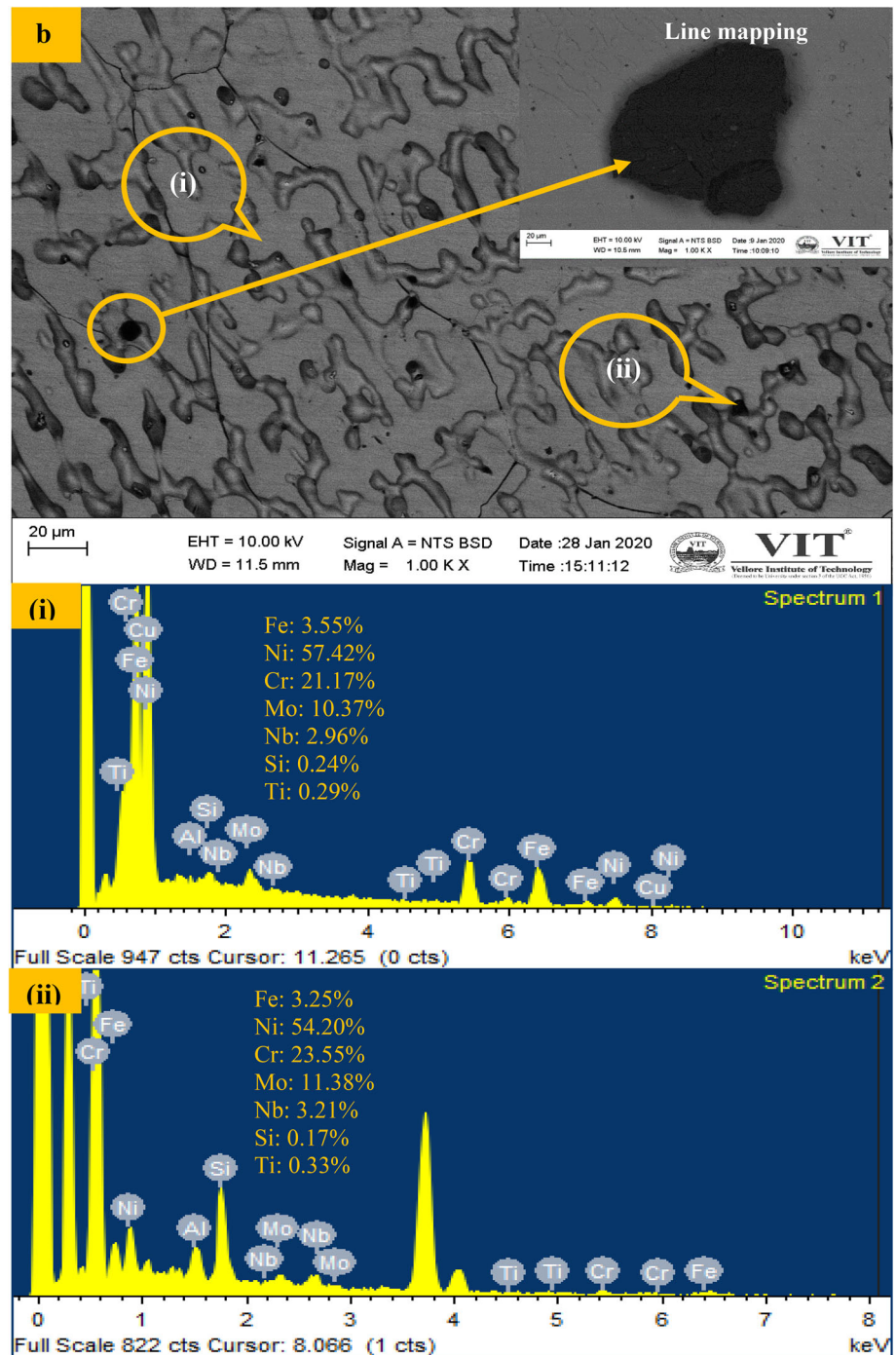


Fig. 13 continued



Filler wires (ERNiCrMo-2 and ERNiCrMo-3) have a higher amount of nickel which enhances the toughness of the weldments. The toughness of PCGTAW ERNiCrMo-2 is marginally higher than all the specimens in this study due to tungsten segregation at the interdendritic regions, and formation of interstitial compounds (Mo_{23}C_6 and MoC) also improve the toughness [23].

SEM fractographic images (Fig. 21) reveal that microvoids with elongated dimple structures are observed in the impact-fractured CCGTAW and PCGTAW specimens. All the CCGTAW specimens are fractured completely as compared to PCGTAW specimens. Ductile mode of fracture is identified from the impact tests, and also SEM images confirm the ductility with dimple structure [24].

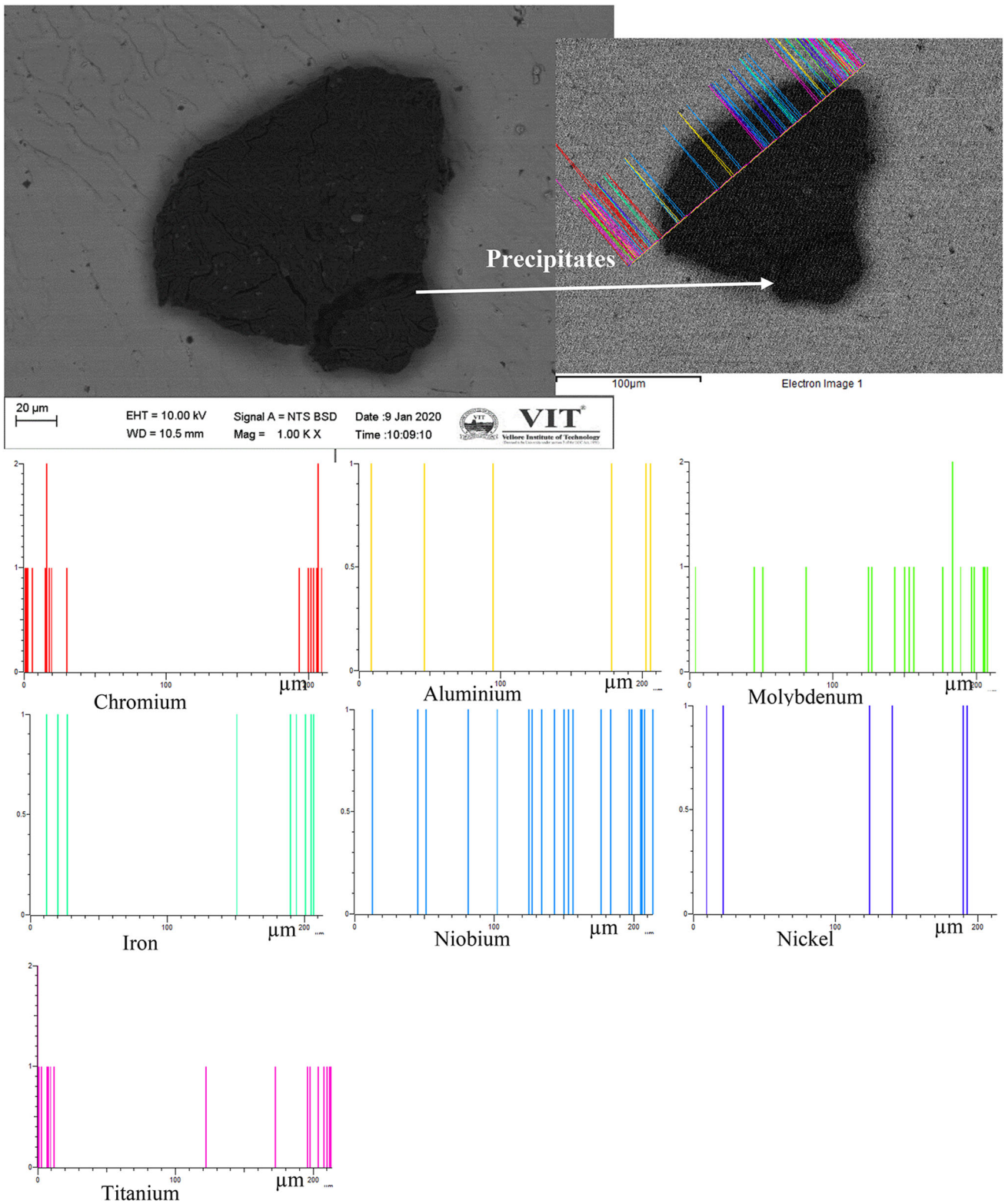


Fig. 14 Line mapping of a precipitate in PCGTAW ERNiCrMo-3 weldment

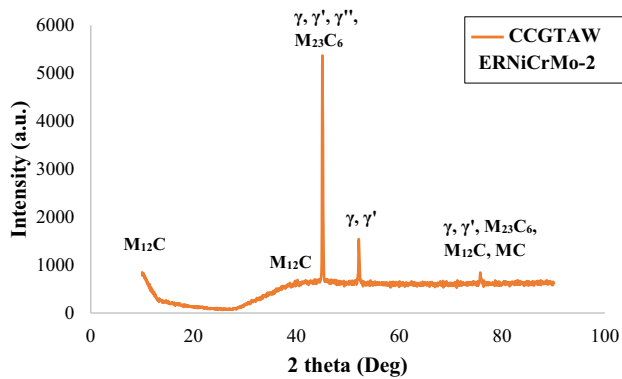


Fig. 15 XRD analysis of CCGTAW ERNiCrMo-2 weldment

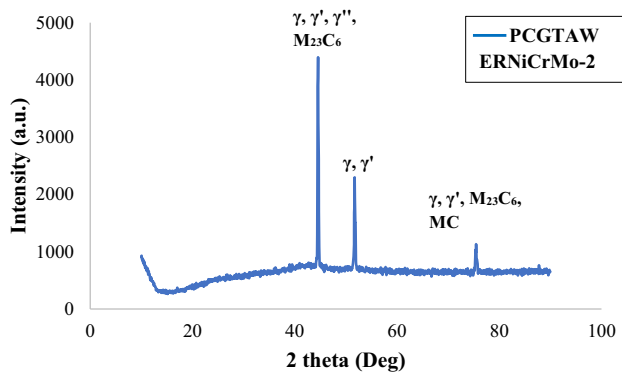


Fig. 16 XRD analysis of PCGTAW ERNiCrMo-2 weldment

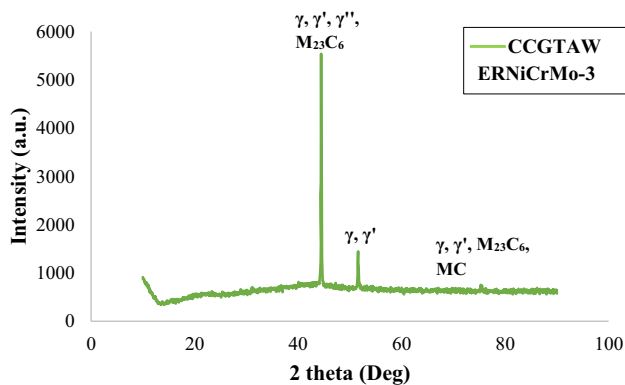


Fig. 17 XRD analysis of CCGTAW ERNiCrMo-3 weldment

3.7 Tensile Results of Incoloy 20 Weldments

Tensile tested specimens of Incoloy 20 weldments with ERNiCrMo-2 and ERNiCrMo-3 filler wires using CCGTAW and PCGTAW are shown in Fig. 22. Average UTS, average YS, and average ductility of CCGTAW and PCGTAW with ERNiCrMo-2 and ERNiCrMo-3 filler wires are listed in Table 4. Fracture of weldments for both fillers is observed at HAZ. Reduction in the thermal gradient at the phase of solidification causes grain growth in

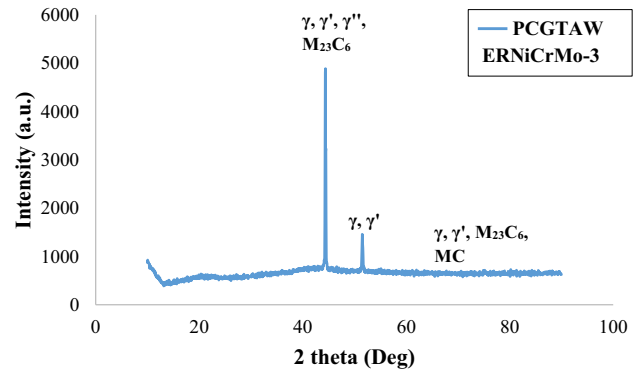


Fig. 18 XRD analysis of PCGTAW ERNiCrMo-3 weldment

the HAZ. Coarsened grains is the reason for the occurrence of fracture at HAZ, and it is also evinced from the hardness test. Higher ultimate tensile strength is achieved in the PCGTAW specimens in comparison with corresponding CCGTAW specimens. Refinement in grain size is also the reason for higher strength and enhanced ductility [22]. EBSD analysis provides a detail microstructure investigation to analyze at the HAZ of all weldments. The fractographic analysis (Fig. 23) is performed for fused specimens using CCGTAW and PCGTAW processes. Microvoids and dimples are found in all the weldments which exhibit the ductile mode of fracture. Ductility is marginally enhanced in PCGTAW specimens due to a reduction in grain size in the HAZ as compared to CCGTAW specimens.

3.8 EBSD Analysis of Incoloy 20 at HAZ

EBSD analysis results of Incoloy 20 at HAZ are presented in Figs. 24, 25, 26 and 27. Image quality (IQ) map (Figs. 24a, 25a, 26a, 27a) reveals an excellent quality microstructure of weldments at HAZ where different grain sizes are observed. In this study, the tensile fracture occurs at HAZ. The difference in the grain size occurs due to the variation in the thermal gradient during the welding process. Inverse pole figure (IPF) map at HAZ exhibits the random orientation of the grains and size at HAZ through the color variation as shown in Figs. 24b, 25b, 26b and 27b. Various sizes and proportions of the grains are observed at HAZ of all the weldments. Grain sizes at HAZ (CCGTAW ERNiCrMo-2 (2.03 to $297.32 \pm 62.6 \mu\text{m}$), PCGTAW ERNiCrMo-2 (2.08 to $167.46 \pm 36 \mu\text{m}$), CCGTAW ERNiCrMo-3 (2.03 to $288.49 \pm 77.13 \mu\text{m}$), and PCGTAW ERNiCrMo-3 (2.01 to $214.169 \pm 38.76 \mu\text{m}$)) are measured using EBSD analysis. Higher heat input coupled with a slower cooling rate is the reason for coarsened grains at HAZ of CCGTAW specimens. Grain boundary (GB) map shows the low-angle boundary (2° to 5°) with the minimum fraction and high-angle boundary (5° to 60°) with maximum fraction at HAZ

Fig. 19 Hardness results of Incoloy 20 weldments

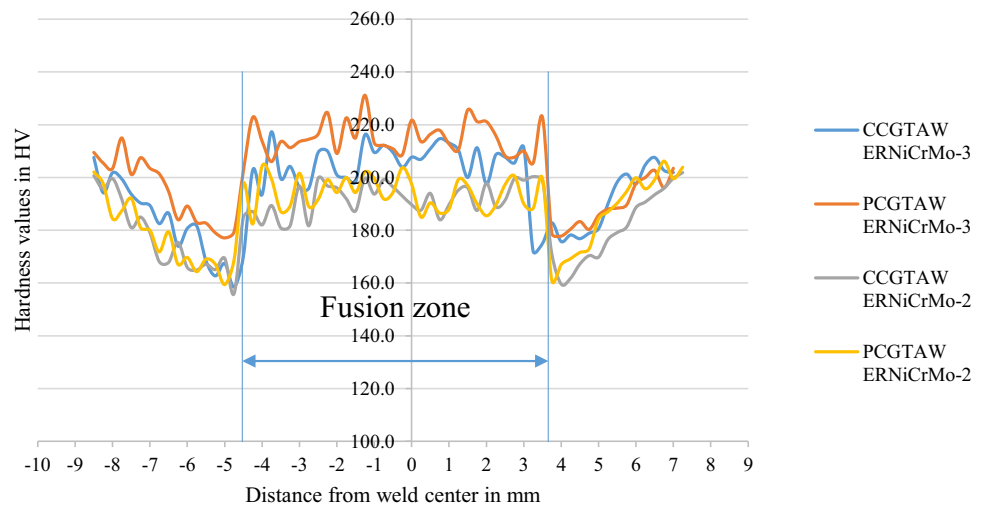


Table 4 Mechanical properties of Incoloy 20 and its weldments

Material	Average hardness of weldments (HV)	Average toughness (J)	Average UTS (MPa)	Average yield strength (MPa)	Average ductility (%)
Base metal	208	119	654	367	47
CCGTAW ERNiCrMo-2	194	111	616	315	37
PCGTAW ERNiCrMo-2	206	126	630	329	38
CCGTAW ERNiCrMo-3	205	98	632	321	38
PCGTAW ERNiCrMo-3	215	112	646	356	41

(Figs. 24c, 25c, 26c, 27c). KAM map exhibits the local misorientation of grain boundaries where local strains or dislocation sites are observed. Local strains are represented in green color. Uneven distribution of local strains is noticed at HAZ as shown in Figs. 24d, 25d, 26d and 27d. These uneven local strains are the reason for failure at HAZ when the tensile force is applied [25].

3.9 Evaluation of Electrochemical Corrosion

Potentiodynamic curves of Incoloy 20 and its weldments are shown in Fig. 28. Electrochemical corrosion test results such as corrosion potential (E_{corr}), corrosion current density (I_{corr}), and corrosion rate (C_{rate}) are listed in Table 5. SEM images of corrosion tested base metal and weldments are shown in Figs. 29, 30, 31, 32 and 33. Corrosive regions are represented as white arrows in the SEM images. In this study, the ranking for corrosion is Incoloy 20 > CCGTAW ERNiCrMo-2 > CCGTAW ERNiCrMo-3 > PCGTAW ERNiCrMo-2 > PCGTAW ERNiCrMo-3. Significant parameters of pitting corrosion are the elemental

composition, electrolyte concentration, electrochemical potential and temperature. The pitting corrosion mechanism involves breakdown or initiation of the pitting of the passive protective layer. The strong protective passive layer forming elements are Ni, Cr, Mo, and Ti [26]. The higher corrosion rate is observed in the Incoloy 20 base metal as compared to ERNiCrMo-2 and ERNiCrMo-3 weldments. The corrosion rate of weldments is lessened due to the higher amount of Ni, Cr, and Mo elements which have a passive protective layer. The difference of corrosion potential (E_{corr}) between the base metal and the weldments is 0.4 mV that lead to the formation of effective galvanic couples and increased the corrosion rate [12].

4 Conclusions

1. Macrostructural observation for Incoloy 20 weldments made with ERNiCrMo-2 and ERNiCrMo-3 filler wires using continuous and pulsed current gas tungsten arc welding processes exhibits crack-free welds.

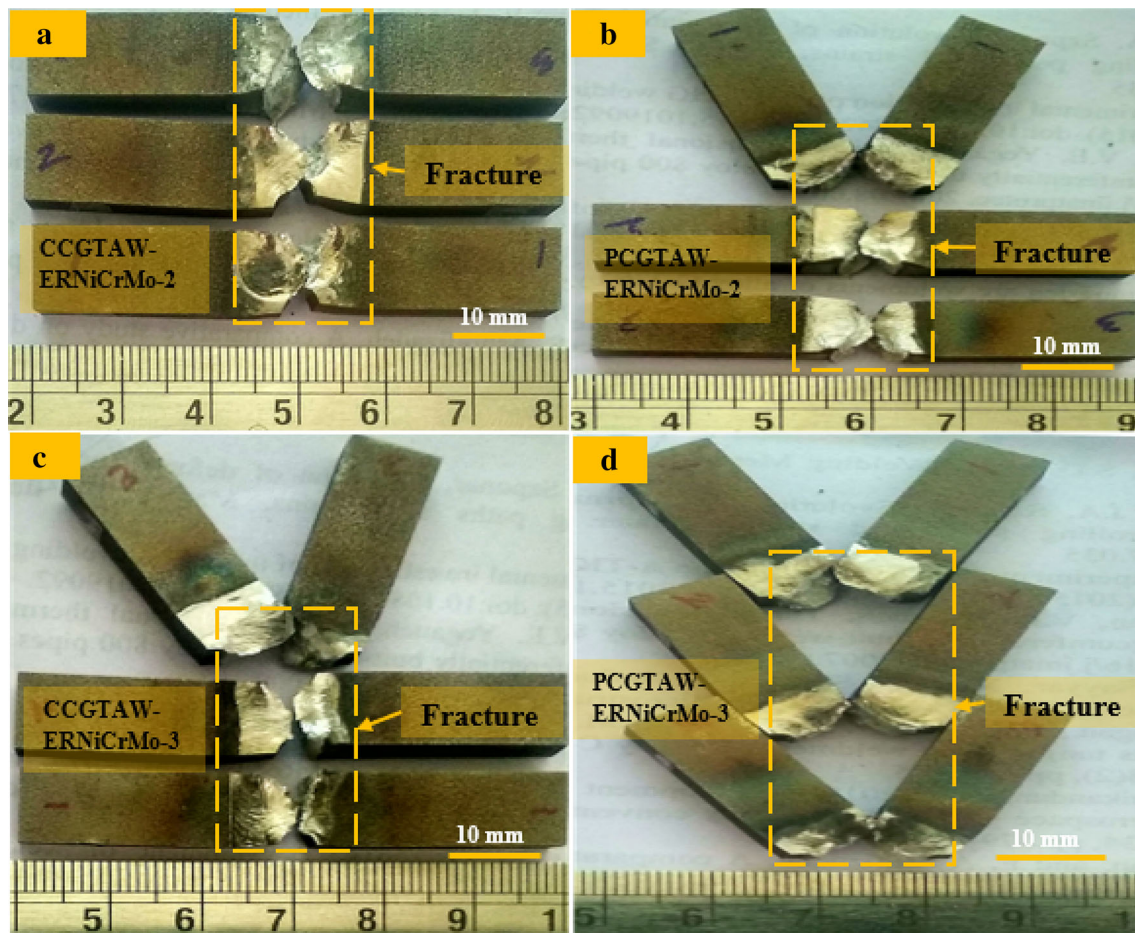


Fig. 20 Toughness values of Incoloy 20 weldments

- The microstructural evaluation shows cellular and columnar grains in CCGTAW specimens and columnar and equiaxed grains in PCGTAW specimens for both filler wires. Coarsened grains at heat-affected zone are found with CCGTAW specimens in comparison with PCGTAW specimens for both filler wires.
- Segregation of chromium has taken place at the stage of solidification in CCGTAW ERNiCrMo-2 and segregation of niobium in the CCGTAW ERNiCrMo-3. Reduced segregation of elements is observed in PCGTAW specimens.
- X-Ray diffraction results reveal intermetallic compounds for CCGTAW ERNiCrMo-2 (Cr_7C_3 and $\gamma\text{-Ni}$), PCGTAW ERNiCrMo-2 ($\gamma\text{-Ni}$ and Ni_3C), CCGTAW ERNiCrMo-3 (Ni_3C , NbNi_3 , and Fe_4C), and PCGTAW ERNiCrMo-3 (MoNi_4 , Ni_3C , and $\gamma\text{-MoC}$).
- Microhardness test exhibits that enhancement of average hardness values of around 4% in the PCGTAW specimen for ERNiCrMo-2 is observed than the corresponding CCGTAW. For ERNiCrMo-3, enhancement of around 6% is observed in the PCGTAW specimen than that of CCGTAW.
- Impact test discloses that toughness values for PCGTAW specimens are improved by around 13% as compared to CCGTAW for ERNiCrMo-2 filler wire. For ERNiCrMo-3, toughness values of PCGTAW specimen are 14% higher than that of CCGTAW.
- The tensile test reveals that the average ultimate tensile strength of PCGTAW specimen is 2% higher than that of CCGTAW for both filler wires. Enhanced mechanical properties are found in PCGTAW specimens for both filler wires as compared to CCGTAW specimens. Improvement in the mechanical and metallurgical properties is observed for PCGTAW specimens for both filler wires due to lessened heat input and a rapid cooling rate.
- The electrochemical corrosion test reveals that higher corrosion resistance is observed in the PCGTAW specimens as compared to CCGTAW specimens.
- From both processes and filler wires, it is recommended that the PCGTAW ERNiCrMo-3 specimen is offering a better outcome for mechanical, metallurgical, and corrosion properties.

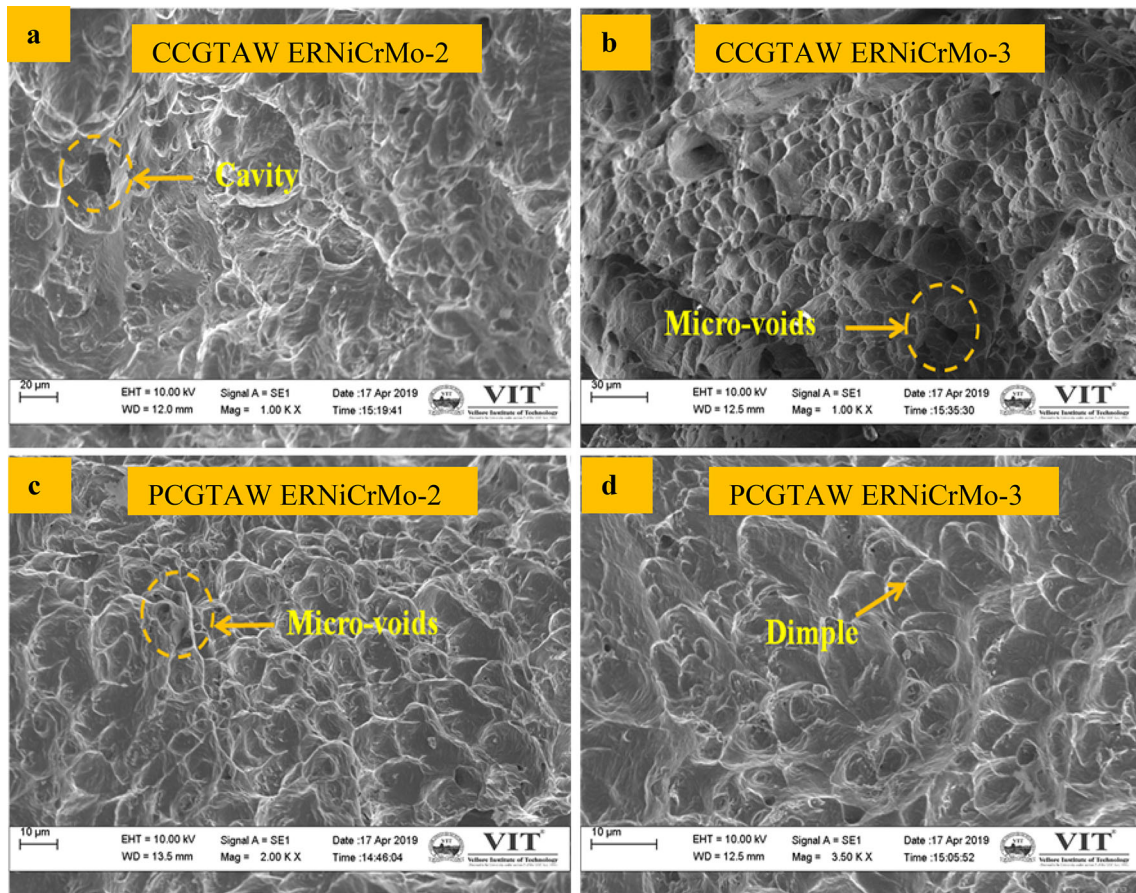


Fig. 21 Fractographic images (Impact fracture) of Incoloy 20 weldments

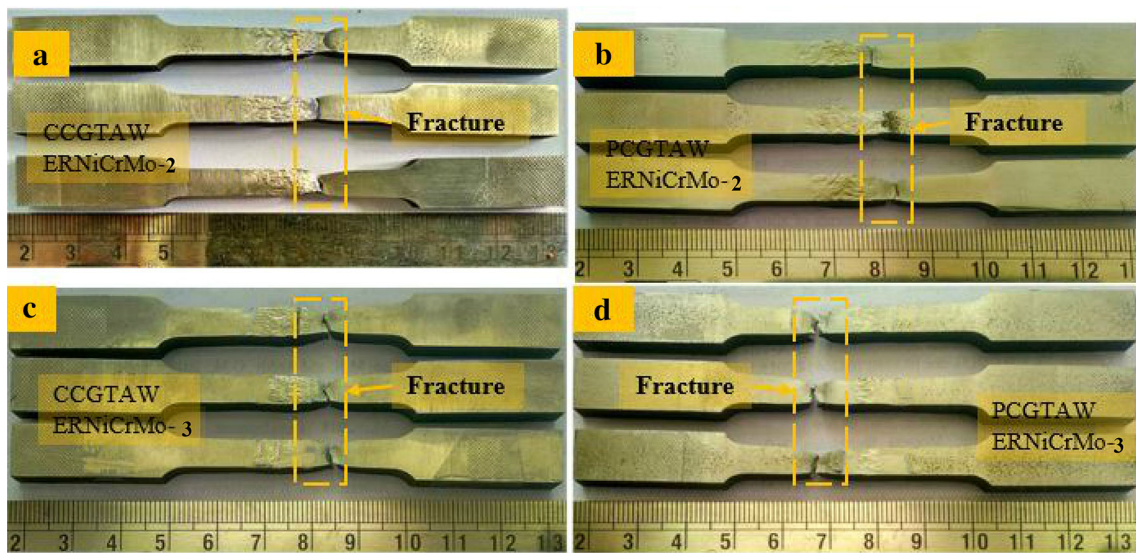


Fig. 22 Tensile fractured specimens of Incoloy 20 weldments

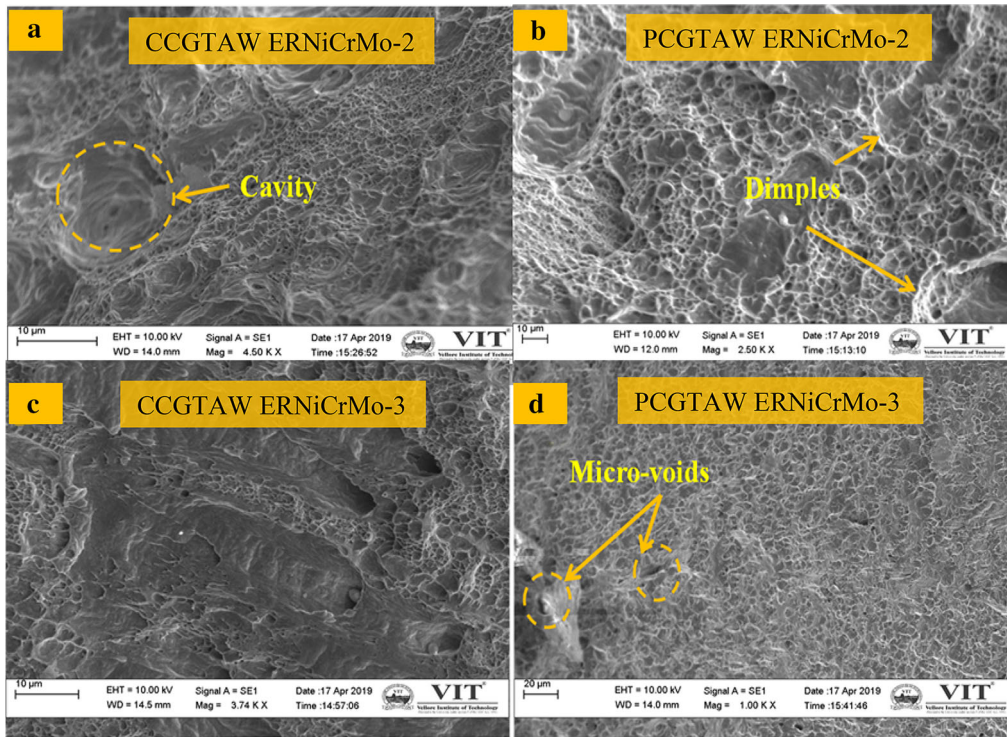


Fig. 23 Tensile fractured specimens of Incoloy 20 weldments

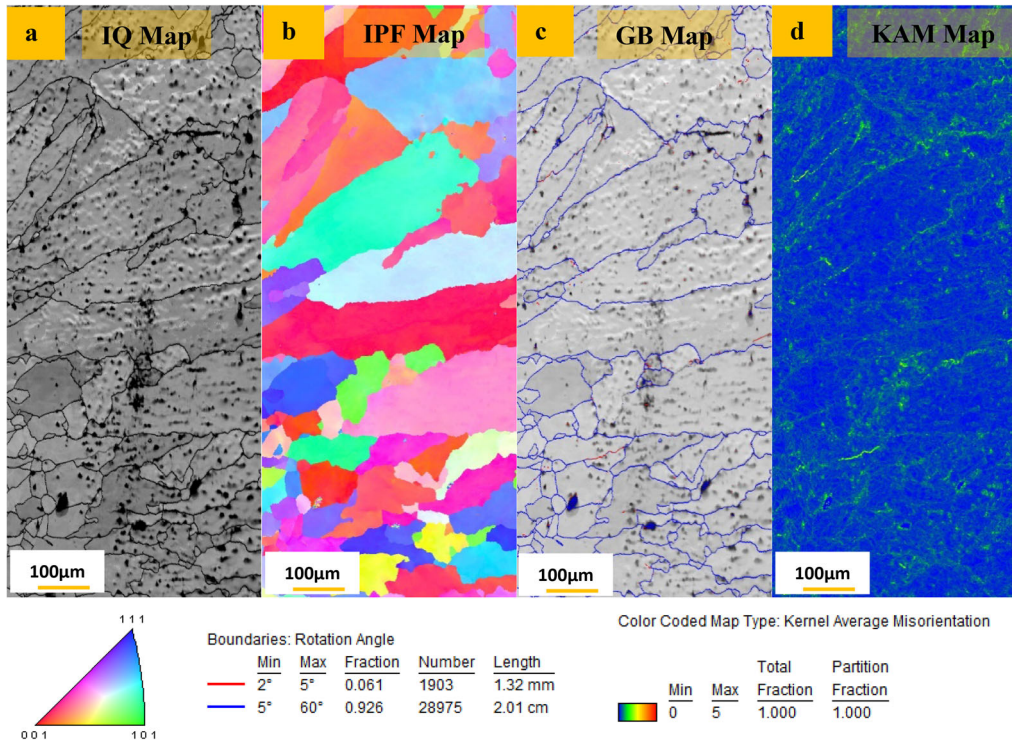


Fig. 24 EBSD analysis of Incoloy 20 weldment with ERNiCrMo-2 using CCGTAW

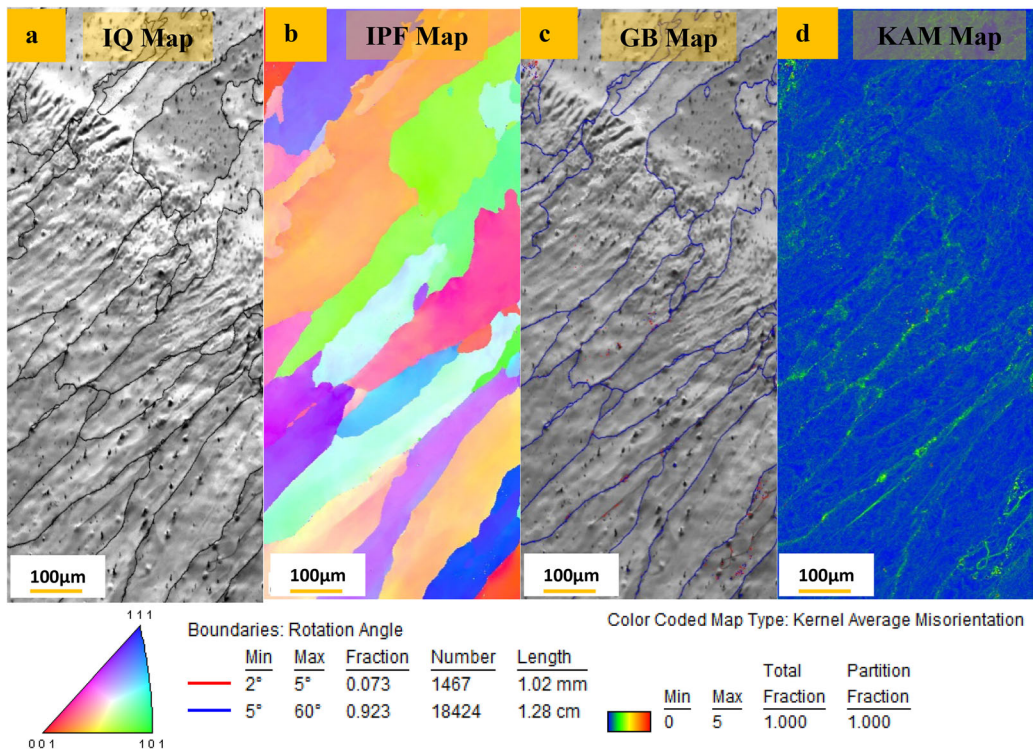


Fig. 25 EBSD analysis of Incoloy 20 weldment with ERNiCrMo-2 using PCGTAW

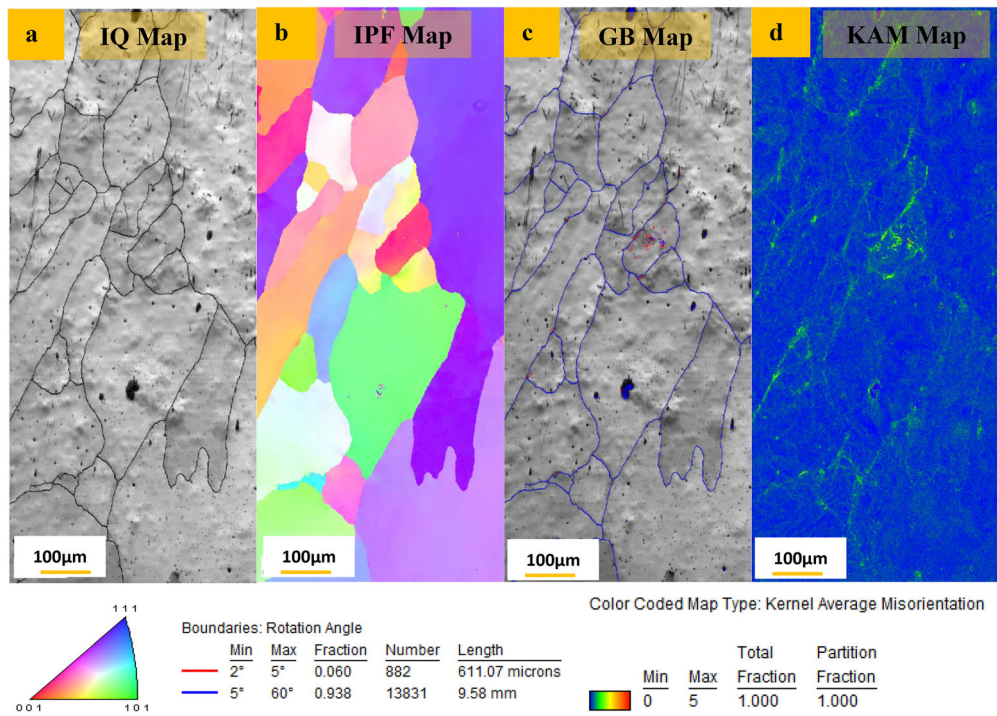


Fig. 26 EBSD analysis of Incoloy 20 weldment with ERNiCrMo-3 using CCGTAW

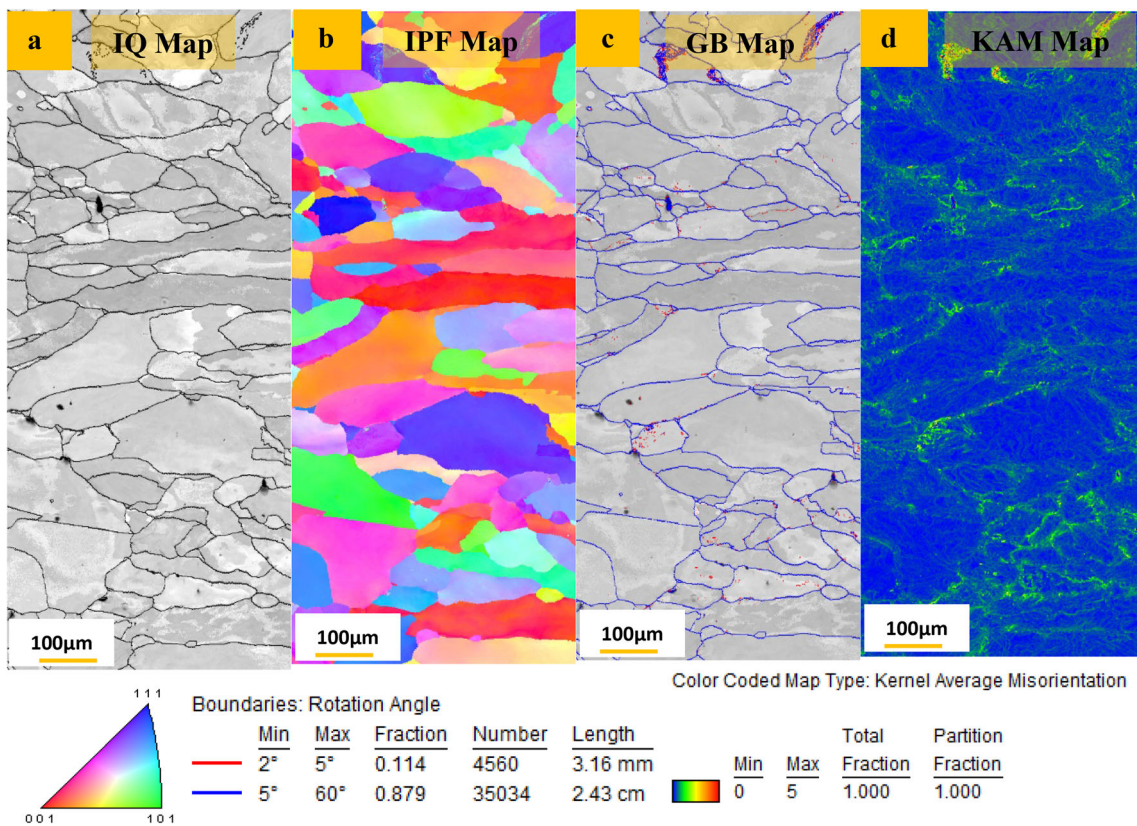


Fig. 27 EBSD analysis of Incoloy 20 weldment with ERNiCrMo-3 using PCGTAW

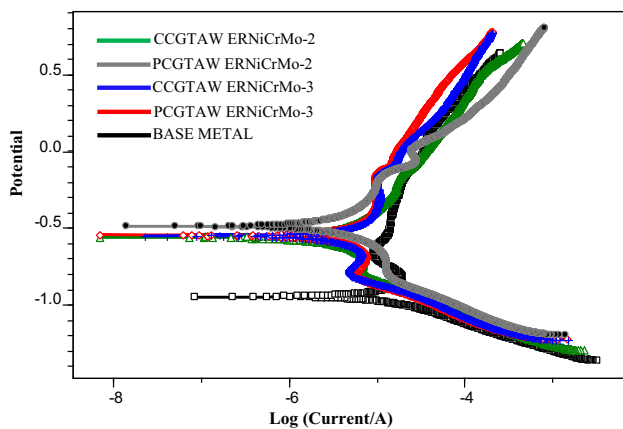


Fig. 28 Potentiodynamic curves of Incoloy 20 weldments

Table 5 Corrosion properties of Incoloy 20 and its weldments

Material	E_{corr} (mV)	I_{corr} (mA cm ⁻²)	C. rate (mm/year)
Base metal	- 0.9543	7.747×10^{-6}	0.07969
CCGTAW ERNiCrMo-2	- 0.5977	4.529×10^{-6}	0.04658
PCGTAW ERNiCrMo-2	- 0.5847	2.628×10^{-6}	0.02703
CCGTAW ERNiCrMo-3	- 0.5060	2.816×10^{-6}	0.02896
PCGTAW ERNiCrMo-3	- 0.5521	2.333×10^{-6}	0.02400

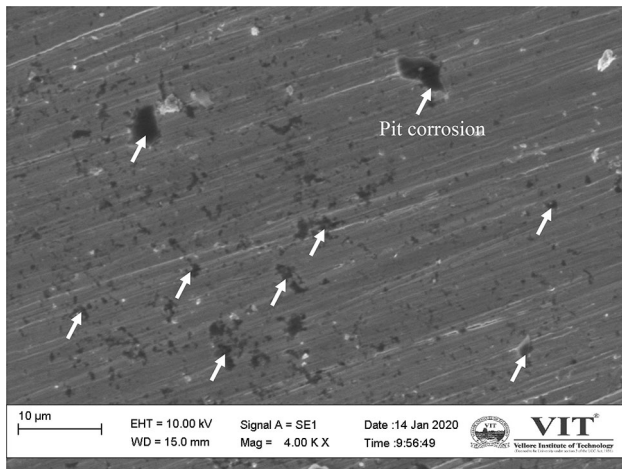


Fig. 29 SEM image of electrochemically corroded Incoloy 20

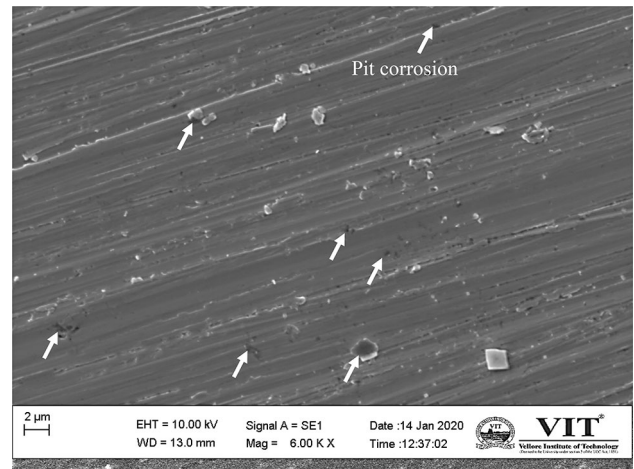


Fig. 32 SEM image of electrochemically corroded CCGTAW ERNiCrMo-3 weldment

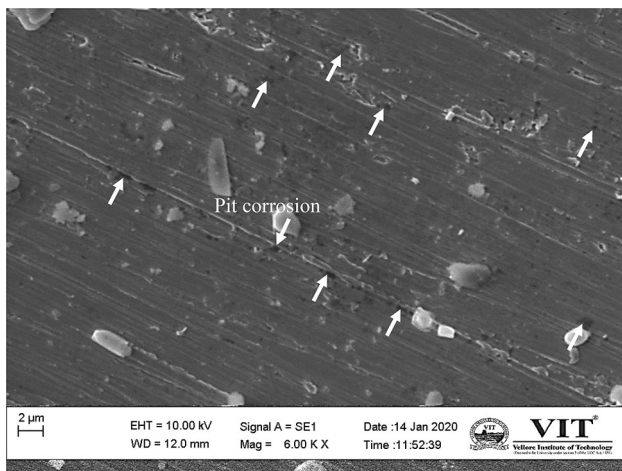


Fig. 30 SEM image of electrochemically corroded CCGTAW ERNiCrMo-2 weldment

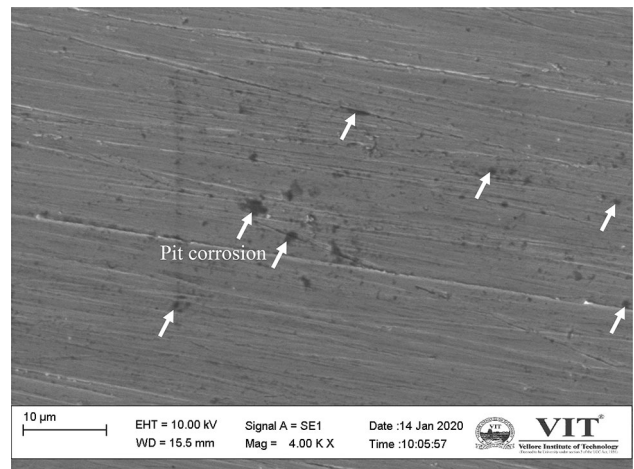


Fig. 33 SEM image of electrochemically corroded PCGTAW ERNiCrMo-3 weldment

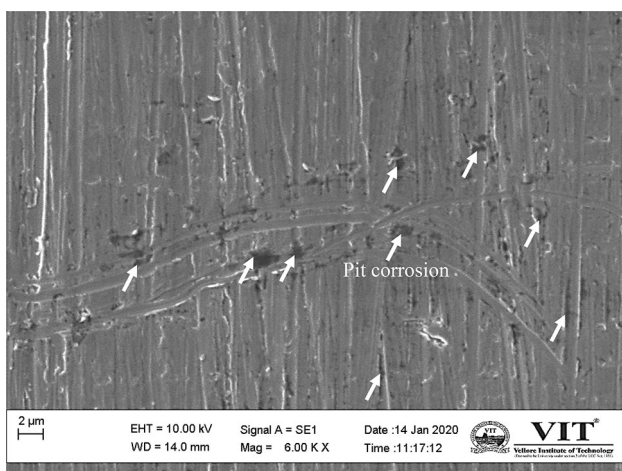


Fig. 31 SEM image of electrochemically corroded PCGTAW ERNiCrMo-2 weldment

Acknowledgements We express our gratitude to VIT, Vellore for giving the VIT SEED GRANT to perform this investigation. And we also thank Mr. Natarajan R, Delta Weartech Engineers Pvt. Ltd., Chennai, for contributing to the experimental part and VIT, Vellore for offering the characterization support through Materials Engineering and Technology Laboratory, Advanced Materials Processing and Testing Laboratory, and Scanning Electron Microscopic Laboratory.

References

1. John DuPont N, Lippold John C, and Samuel Kiser D, *Welding metallurgy and weldability of nickel-base alloys*, A John Wiley & Sons, USA (2011).
2. INCOLOY alloy 20, Technical data sheet, Special Metals Corporation. <http://www.specialmetals.com/assets/smc/documents/alloys/incoloy/incoloy-alloy020.pdf>. Accessed 23 Apr 2019.

3. Kangazian J, Sayyar N and Shamanian M, *J Metallogr Microstruct Anal* **6** (2017) 190. <https://doi.org/10.1007/s13632-017-0353-x>.
4. Bernasovsky P, *Weld Int* **3** (1989) 814. <https://doi.org/10.1080/09507118909446666>.
5. Sayyar N, Shamanian M and Niroumand B, *J Mater Process Technol* **262** (2018) 562. <https://doi.org/10.1016/j.jmatprotec.2018.07.020>.
6. Sayiram G and Arivazhagan N, *Mater Char* **102** (2015) 180. <https://doi.org/10.1016/j.matchar.2015.03.006>.
7. Kangazian J and Shamanian M, *Mater Char* **155** (2019) 109802. <https://doi.org/10.1016/j.matchar.2019.109802>.
8. Dehmlaei R, Shamanian M and Kermanpur A, *Mater Char* **59** (2008) 1447. <https://doi.org/10.1016/j.matchar.2008.01.013>.
9. Kermanpur A, Shamanian M and EsfahaniYeganeh V, *J Mater Process Technol* **199** (2008) 295. <https://doi.org/10.1016/j.jmatprotec.2007.08.009>.
10. Stescu C, Munteanu C, Luca D, Istrate B, Benchea M, Chicet D and Oprisan B, *Mater Sci Forum* **907**(2017) 145. <https://doi.org/10.4028/www.scientific.net/MSF.907.145>.
11. Srikanth A and Manikandan M, *J Manuf Process* **30** (2017) 452. <https://doi.org/10.1016/j.jmapro.2017.10.014>.
12. Derakhshi M A, Kangazian J, and Shamanian M, *Vacuum* **161** (2019) 371. <https://doi.org/10.1016/j.vacuum.2019.01.005>.
13. Mani C, Karthikeyan R, and Kannan S, *Metals* **9** (2019): 1088. <https://doi.org/10.3390/met9101088>.
14. Aghaie-Khafri M and Golarzi N, *Mater Sci Eng A* **486** (2008) 641. <https://doi.org/10.1016/j.msea.2007.11.059>.
15. Wu S J, Du C W and Kuo C M, *Mater Sci Forum* **638** (2010) 2499. <https://doi.org/10.4028/www.scientific.net/MSF.638-642.2499>.
16. Subramani P and Manikandan M, *J Manuf Process* **34** (2018) 579. <https://doi.org/10.1016/j.jmapro.2018.06.037>.
17. Manikandan M, Arivazhagan N, Nageswara Rao M and Madhusudhan Reddy G, *J Manuf Process* **16** (2014) 563. <https://doi.org/10.1016/j.jmapro.2014.08.002>.
18. Kou S, *Welding metallurgy*, New Jersey: USA (2003).
19. Romig A D, Lippold J C, and Cieslak M J, *Metall Trans A* **19** (1988) 35. <https://doi.org/10.1007/BF02669813>.
20. Lingenfelter A C, International Nickel Co Inc Huntington. W. Va (1972).
21. Taheri N, Naffakh-Moosavy H, Ghaini F M, *Opt Laser Technol* **91** (2017) 71. <https://doi.org/10.1016/j.optlastec.2016.12.013>.
22. Manikandan S G K, Sivakumar D, Prasad Rao K, Kamaraj M, *J Mater Process Technol* **214** (2014) 3141. <https://doi.org/10.1016/j.jmatprotec.2014.07.022>.
23. Kim J K, Park H J, Shim D N, *Acta Metall Sin (Engl Lett)* **29** (2016) 1107. <https://doi.org/10.1007/s40195-016-0494-y>.
24. Arulmurugan B and Manikandan M, *Mater Sci Eng A* **691** (2017) 126. <https://doi.org/10.1016/j.msea.2017.03.042>.
25. Schwartz A J, Kumar M, Adams BL, Field DP, New York; Kluwer Academic (2000).
26. Loto R T, *New Aspects* (2017) 147. <https://dx.doi.org/10.5772/intechopen.70579>.

Publisher's Note Springer Nature remains neutral with regard to jurisdictional claims in published maps and institutional affiliations.